

A comprehensive study of ALPs from B -decays

Deepanshu Bisht[✉], Sabyasachi Chakraborty[✉], and Atanu Samanta[✉].

Department of Physics, Indian Institute of Technology Kanpur, Uttar Pradesh-208016, India

E-mail: dbisht22@iitk.ac.in, sabyac@iitk.ac.in, asamanta23@iitk.ac.in

ABSTRACT: We present a comprehensive study of axion-like particles (ALPs) through flavor changing neutral current processes, such as $B \rightarrow Ka$ followed by hadronic decays. Our generic framework encompasses different ultraviolet scenarios similar to KSVZ, DFSZ and Flaxion etc. Starting from the effective Lagrangian written at the high scale, we compute the anomalous dimension matrix, taking into account all one-loop and relevant two-loop contributions. The latter is most important for the KSVZ and heavy QCD axion scenarios. We recognized that such two-loop diagrams can have both ultraviolet (UV) and infrared (IR) divergences. We show explicitly that UV divergences cancel by inserting appropriate counterterms, which are new operators involving the axion field and required to be present at the UV itself, to renormalize the theory. On the other hand, the cancellation of IR divergences is subtle and demonstrated through matching with the effective theory at the electroweak scale. We also utilize chiral perturbation theory and vector meson dominance framework to compute the decay and branching fractions of the ALP pertaining to our framework. We find that for KSVZ-like scenario, axion decay constant, $f_a \lesssim 1$ TeV can be ruled out. The bound becomes stronger for the DFSZ and Flaxion-like models, reaching upto 10^2 TeV and 10^3 TeV respectively. We also provide projections on the parameter space based on 3 ab^{-1} data from Belle II.

Contents

1	Introduction	2
2	The Effective Lagrangian	5
3	Renormalization Group Evolutions	6
3.1	Generic Framework	6
3.2	Anomalous dimension matrix	9
3.3	Counterterms	17
3.4	Complete set of RGEs	19
4	Finite terms	19
5	Matching at the Electroweak Scale	21
5.1	Generic Wilson coefficients of the EFT	21
5.2	Evaluation of C'_{4L}	22
6	Axion Decays and Branching Fractions	25
7	Experimental Searches and Projections	27
7.1	Inclusive $b \rightarrow sa$ process	27
7.2	Present Constraints	27
7.3	Future Projections	28
8	Results and Discussions	29
8.1	KSVZ-Like Model	29
8.2	DFSZ-Like Model	31
8.3	Flavorful Axion Model	33
9	Conclusion	34
A	Interaction vertices	36
B	Example of a two-loop amplitude	36
C	Bounds for KSVZ-Like scenario ($\Lambda = 4\pi f_a$)	38
D	Input Parameters	39
E	Axion decay width	39

1 Introduction

Searches for new physics significantly lighter than the TeV scale have garnered considerable attention in the recent past. The reason is primarily twofold: Firstly, the lack of any signatures of new physics at the Large Hadron Collider (LHC) has prompted us to pursue a broader perspective on where new physics could hide. Secondly, any new light physics particles offer the potential to be tested at multiple frontiers, such as intensity, cosmic frontier, etc. The axion [1, 2] is one of the most well-motivated and well-studied example for such light new physics. They usually emerge as pseudo-Nambu-Goldstone bosons resulting from the spontaneous breaking of a $U(1)$ symmetry, for example, the Peccei-Quinn (PQ) symmetry [3, 4] and hence are naturally light. The QCD-induced potential of the axion is naturally minimized at the zero expectation value of the axion field, providing a compelling solution to the strong- CP problem [5]. Over the years, the axion has been demonstrated to be an excellent cold dark matter candidate [6–8], resolve the matter-antimatter asymmetry [9, 10] and, in some incarnations, address the long-standing hierarchy problem of the Standard Model (SM) [11–13]. As a result, the axion provides a natural testing ground for physics beyond the SM.

For a prototypical axion, QCD solely determines its mass, predicting the relation $m_a f_a \simeq m_\pi f_\pi$, where, like pions, m_a and f_a are the mass and decay constants for the axion. It is important to note that f_a also indicates the scale at which the PQ symmetry

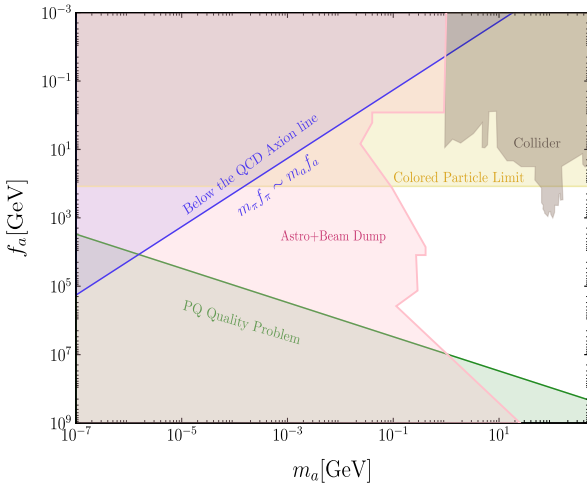


Figure 1. A schematic representation of axion parameter space inspired from [14]. Colored regions are ruled out by different frontier experiments.

is spontaneously broken. Although f_a could theoretically take any value, it is rather well motivated from both theoretical and experimental perspectives to choose it around the TeV scale. However, such a choice automatically places the axion mass around the keV scale, which is already excluded by astrophysical observations [15–18] and beam dump experiments [19–22]. Furthermore, the straightforward and elegant bottom-up solution to the strong- CP problem suffers from a major top-down flaw. The QCD-induced potential is extremely shallow. As a result, any explicit PQ symmetry-breaking effects, even those suppressed by the Planck scale, such as $V \sim f_a^5/M_{Pl} \lesssim \Lambda_{\text{QCD}}^4$ can shift the minima of the potential away from zero, thus jeopardizing the solution of the strong- CP problem. This particular issue is known as the axion quality problem in the literature [23–26]. It therefore becomes imperative to choose frameworks that deviate away from the aforementioned mass relation. This can be realized by considering an additional contribution to the axion potential. Several model building efforts have been made in this direction in the recent past [14, 27–44], giving

is spontaneously broken. Although f_a could theoretically take any value, it is rather well motivated from both theoretical and experimental perspectives to choose it around the TeV scale. However, such a choice automatically places the axion mass around the keV scale, which is already excluded by astrophysical observations [15–18] and beam dump experiments [19–22]. Furthermore, the straightforward and elegant bottom-up solution to the strong- CP problem suffers from a major top-down flaw. The QCD-induced potential is extremely shallow. As a result, any explicit PQ symmetry-breaking effects, even those suppressed by the Planck scale, such as $V \sim f_a^5/M_{Pl} \lesssim \Lambda_{\text{QCD}}^4$ can shift the minima of the potential away from zero, thus jeopardizing the solution of the strong- CP problem. This particular issue is known as the axion quality problem in the literature [23–26]. It therefore becomes imperative to choose frameworks that deviate away from the aforementioned mass relation. This can be realized by considering an additional contribution to the axion potential. Several model building efforts have been made in this direction in the recent past [14, 27–44], giving

rise to axion-like particles (ALPs). It is evident that higher mass axions or lower values of the $f_a \sim \mathcal{O}(\text{TeV})$ scale not only reintroduce the advantages of electroweak scale axion but also ameliorate the quality problem. Indeed, such a region (see Fig. 1) with $m_a \gtrsim \mathcal{O}(\text{MeV})$ and $f_a \gtrsim \mathcal{O}(\text{TeV})$ has yet to be probed by experiments. Moreover, slightly heavier axions around the GeV scale also present considerable theoretical challenges, which is the primary focus of our work.

Such regions are also ideally suited for intensity frontier experiments, which utilize intense sources of beam to investigate rare processes in the SM. The main advantage is that, since SM processes are rare, any potential new physics might not be masked by a large SM background. Motivated by this, we will focus on axion-like particles with $f_a \sim \mathcal{O}(\text{TeV})$ and which predominantly couple to the SM gluon and quark fields. As a result, both the production and the decay modes of these ALPs would be mainly hadronic [45]. For ALP masses $m_a \lesssim \mathcal{O}(\text{GeV})$, it is convenient and customary to rotate away the axion-gluon $a - G - \tilde{G}$ term in the Lagrangian by performing a chiral transformation on the SM quark fields. Under chiral rotation, the measure of the action is not invariant and can be chosen to completely rotate away the axion-gluon term. The subsequent Lagrangian generates the axion-quark mass and kinetic mixing terms, which can be matched with the effective theory of the Chiral Lagrangian (ChPT) [46–48]. This effective potential derived from the Chiral Lagrangian is well suited to study non-perturbative effects such as $a - \pi^0$ and $a - \eta(\eta')$ mixing. This framework is frequently used to probe the axion parameter space by studying rare decays of pions [48–51] and kaons [47, 52–59]. Similarly, fixed-target experiments [60, 61] and colliders [62–68] also provide competitive constraints in the $m_a - f_a$ plane, albeit for slightly heavier masses. Noticeably, for $m_a \gtrsim \mathcal{O}(\text{GeV})$, the power counting of the ChPT breaks down, necessitating perturbative calculations.

The region with $\mathcal{O}(100 \text{ MeV}) \lesssim m_a \lesssim \mathcal{O}(\text{GeV})$ is also sensitive to flavor-changing neutral current (FCNC) processes, mostly from decays of the B meson, and can leave telltale signatures. Before discussing the primary objective of our work, let us briefly chart various attempts that have been made to probe such heavy axions in this particular ballpark using FCNC processes.

- **Generic ALP framework:** Ref. [69] presented a relevant anomalous dimension matrix for the most general dimension-5 interactions of axion and SM fields. Partial two-loop matching coefficients were also worked out for flavor-changing effects. This framework was extended to comprehensively study quark and lepton flavor violations [70] in different low-energy experiments.
- **Heavy QCD axion:** Starting from a heavy QCD axion that only couples to gluon fields, ref. [71] studied for the first time, $b \rightarrow s$ transitions generated at the two-loop order. To renormalize the theory, one requires additional counterterms, essentially operators involving axion and quark fields. After the RG evolution of the Wilson coefficients to the weak scale, branching ratios for $B \rightarrow Ka$ were computed and augmented with the decay of the axions. The associated branching fractions of axions were taken from [45], which prescribed a data-driven approach. The bounds obtained both from prompt

searches [71] and displaced vertex searches [72] were demonstrated to be quite robust and conservative, as flavor-changing couplings were not considered in UV.

- **Flavorful axions:** Flavor-dependent axion or Flaxion are also well motivated, as they can address the strong CP problem, as well as the flavor hierarchy of the SM in the quark and lepton sector [73]. This is usually achieved by augmenting the SM with a complex scalar field. Although the Flaxion can also explain the observed dark matter abundance [74] and baryon asymmetry, the radial mode or flavon can play the role of an inflaton. Similar frameworks where axions possess non-universal PQ charges [75–77] as well as Froggatt-Nielson [78] motivated frameworks where ALPs only interact with up-type quarks [79] can also provide interesting discovery potential at the B -factories and other low energy experimental facilities.

Other studies of heavier ALP searches using FCNC processes involve ALP coupling to weak gauge SM bosons [80], exploring the interplay of ALP-Higgs and bosonic couplings [81] etc. In this paper, we take a similar approach as presented in [71] with the following differences. The minimal heavy QCD axion generates a flavor-changing neutral current process at the two-loop order. Such diagrams can give rise to ultraviolet (UV), infrared (IR), and UV-IR mixed divergences. Working in the dimensional regularization scheme with the $\overline{\text{MS}}$ scheme, we show that the UV and UV-IR mixed divergences are canceled by incorporating appropriate counterterms. Meanwhile, the purely IR divergences cancel through the process of matching with the effective theory written at the electroweak scale. In addition to the full two-loop and one-loop matching coefficients, we also improved the previous analysis by computing additional pieces in the anomalous dimension matrix. This helps us to consider different UV complete scenarios motivated by KSVZ (Kim-Shifman-Vainshtein-Zakharov) [82, 83], DFSZ (Dine-Fischler-Srednicki-Zhitnitsky) [84, 85] and Flaxions [73]. In contrast, [71] only considered the most minimal case of heavy QCD axions. We emphasize that we only consider the UV values of the Wilson coefficients from these frameworks while deviating away from the axion-pion mass relation. From the perspective of phenomenology, we present limits and projections for these frameworks by including only prompt signatures of ALPs. A detailed study on the displaced vertex signatures will be treated separately.

We organize the paper in the following way. Section 2 presents the effective Lagrangian pertinent to the study of the $b \rightarrow s$ transition in the context of an ALP. This is followed by a discussion of the renormalization group equations in Section 3. We provide a detailed analysis of the dominant contributions to the anomalous dimension matrix. We emphasize that heavy QCD axions contribute to the $b \rightarrow s$ transition at the two-loop level. The cancellation of UV divergences is explicitly demonstrated through counterterms. These counterterms are nothing but operators defined at the UV scale itself, which renormalizes the theory. Once identified, we calculate upto the leading two-loop contribution to the anomalous dimension matrix and compute the renormalization group evolutions of the Wilson coefficient of such operators. This is most relevant for the heavy QCD axion and KSVZ-like scenarios, where at low energy the dominant interaction comes from the axion-gluon interaction. The finite terms of these two loop diagrams are presented in Section 4, which also contains purely IR divergent pieces. In Section 5, we explicitly show

the cancelation of IR divergences by matching the theory to the effective theory at the electroweak scale M_W , as the IR divergence is the same between the two frameworks. After computing the matching coefficients up to two-loop order, in Section 6 we provide results of the axion decay widths and branching fractions for the hadronic decay modes. The detailed discussion can be found in the Appendix E. Next, we discuss the experimental methodologies for the relevant decay channels considered in our analysis in Section 7. This is followed by the presentation of the current and projected exclusion limits in the $m_a - f_a$ plane for several well-motivated UV frameworks such as KSVZ, DFSZ, etc. in Section 8. We consider different scenarios in which the UV scale is independent of f_a , as well as $\Lambda_{UV} = f_a$ or $4\pi f_a$. Finally, we conclude our findings in Section 9. In this work, we focus mainly on the hadronic production and decay modes of ALPs. However, the leptonic modes of ALPs, particularly the displaced signature, can be very interesting. We leave that for future investigations.

2 The Effective Lagrangian

As mentioned in the Introduction, we start with an ALP, where $m_a \gg m_\pi f_\pi / f_a$. The effective Lagrangian takes the form

$$\mathcal{L} = \mathcal{L}_{\text{SM}} + \frac{1}{2} (\partial_\mu a)^2 - \frac{m_a^2}{2} a^2 + \sum_i \mathcal{C}_i \mathcal{O}_i, \quad (2.1)$$

where \mathcal{L}_{SM} denotes the SM Lagrangian, and \mathcal{C}_i 's are the Wilson Coefficients corresponding to the operators \mathcal{O}_i . Notice that the bare-mass term for the axions breaks the axion-pion mass relation. At a fundamental level, this also breaks the shift symmetry, which might jeopardize the solution to the strong- CP problem, requiring an appropriate shift in the axion field itself [86].

For our $b \rightarrow sa$ study, the relevant operators (14 in total) are defined as

$$\begin{aligned} \mathcal{O}_1 &= \frac{a}{f_a} G_{\mu\nu}^b \tilde{G}^{\mu\nu b}, & \mathcal{O}_{2L/R}^i &= \frac{\partial_\mu a}{f_a} \bar{u}_i \gamma^\mu P_{L/R} u_i, \\ \mathcal{O}_{3L/R}^i &= \frac{\partial_\mu a}{f_a} \bar{d}_i \gamma^\mu P_{L/R} d_i, & \mathcal{O}_{4L} &= \frac{\partial_\mu a}{f_a} \bar{s} \gamma^\mu P_L b, \end{aligned} \quad (2.2)$$

where $\tilde{G}^{\mu\nu b} \equiv \frac{1}{2} \epsilon^{\mu\nu\rho\sigma} G_{\rho\sigma}^b$, with $G_{\mu\nu}^b$ being the field strength tensor for the gluon fields¹, while i is a generation index running over up- or down-type quark flavors. Here, $P_L = (1 - \gamma_5)/2$ and $P_R = (1 + \gamma_5)/2$. In this work, L and R will denote left- and right-handed states, respectively.

Note that these operators are generated at the new physics scale Λ_{UV} . For prototypical QCD axions, the coefficient $\mathcal{C}_1 = \alpha_s/8\pi$ arises from the BSM fermion triangle loop. Although our operators can be generalized to include various off-diagonal quark flavors, we have restricted our analysis to couplings pertinent to $b \rightarrow sa$ phenomenology. Motivated

¹Apart from the operators mentioned in Eq. (2.2), axions can also have leptonic as well as Wess-Zumino-Witten (WZW) interactions [87, 88] (also see [89–91] for SM WZW interactions). We ignore them as they do not play any significant role in the construction or phenomenology under consideration.

by experimental searches, we specifically choose all up- and down-sector diagonal quark couplings with ALPs and a single down-sector off-diagonal coupling $b - s - a$.

3 Renormalization Group Evolutions

The Wilson coefficients, defined at the UV scale, must evolve to the electroweak scale using the renormalization group equations (RGE). Since the observations are at the B -physics scale, these operators, in principle, would run again after matching, from the electroweak scale M_W to the bottom mass scale m_b . Following the notation of [92, 93], in this section, we first establish the general framework for the RGEs applicable to composite operators and then specifically address the RGEs relevant to the process under consideration.

3.1 Generic Framework

Renormalization of the fields is required to remove any divergences associated with the computation of a matrix element, such as

$$G_\mu^b{}^{(0)} = \mathcal{R}_{gg}^{1/2} G_\mu^b \approx \left(1 + \frac{1}{2} \delta \mathcal{R}_{gg} \right) G_\mu^b, \quad (3.1)$$

$$q_{L,i}^{(0)} = \left[\mathcal{R}_{q,L}^{1/2} \right]_{ij} q_{L,j} \approx \left[I + \frac{1}{2} \delta \mathcal{R}_{q,L} \right]_{ij} q_{L,j}, \quad (3.2)$$

$$q_{R,i}^{(0)} = \left[\mathcal{R}_{q,R}^{1/2} \right]_{ij} q_{R,j} \approx \left[I + \frac{1}{2} \delta \mathcal{R}_{q,R} \right]_{ij} q_{R,j}, \quad (3.3)$$

where I is an Identity matrix, and q 's are the up or down type quark fields with a generation index i . This wavefunction renormalization relates bare fields to renormalized fields. We do not consider any axion field renormalization, as it is suppressed by additional powers of f_a .

In addition, composite operators such as defined in Eq. (2.2) often give rise to other divergent contributions and hence require operator renormalization described by [93]

$$\mathcal{O}_i^{(0)} = \mathcal{Z}_{ij} \mathcal{O}_j. \quad (3.4)$$

Here, the superscript (0) denotes operators composed of bare fields, while the absence of a superscript indicates renormalized operators. Consequently, the bare and renormalized amputated Green functions, defined by $\langle \dots \rangle$, are connected by the following relationship:

$$\langle \mathcal{O}_i \rangle = \mathcal{Z}_{ij}^{-1} \mathcal{R}_{jk} \langle \mathcal{O}_k \rangle^{(0)} \Rightarrow \langle \mathcal{O}_i \rangle^{(0)} = \mathcal{R}_{ij}^{-1} \mathcal{Z}_{jk} \langle \mathcal{O}_k \rangle = \chi_{ik} \langle \mathcal{O}_k \rangle. \quad (3.5)$$

Here \mathcal{R} is the wavefunction renormalization matrix of the composite operators. The complete renormalization matrix χ , introduced above, is defined as $\chi \equiv \mathcal{R}^{-1} \mathcal{Z}$ and renormalizes the matrix elements (amputated Green functions with insertion of operators). Finally, the effective UV amplitude can be written in terms of the renormalized matrix elements as

$$\mathcal{M}_{\text{UV}} = \mathcal{C}_j \langle \mathcal{O}_j \rangle = \mathcal{C}_j \mathcal{Z}_{jk}^{-1} \mathcal{R}_{ki} \langle \mathcal{O}_i \rangle^{(0)}. \quad (3.6)$$

On the other hand, the running of the Wilson coefficients $\mathcal{C}_i = (\mathcal{C}_1, \mathcal{C}_2, \dots)$ can be deduced by renormalizing in a distinct but equivalent procedure. The relationship between the bare and the renormalized Wilson coefficients is governed by the renormalization matrix \mathcal{Z}_{ij}^c , which is defined by

$$\mathcal{C}_i^{(0)} = \mathcal{Z}_{ij}^c \mathcal{C}_j . \quad (3.7)$$

In this approach, instead of operator renormalization, one uses the *counterterm* method, leading to a finite renormalized effective amplitude

$$\mathcal{M}_{\text{UV}} = \mathcal{C}_j \mathcal{Z}_{kj}^c \mathcal{R}_{ki} \langle \mathcal{O}_i \rangle^{(0)} . \quad (3.8)$$

Compared with Eq. (3.6), we see $\mathcal{Z}_{kj}^c = \mathcal{Z}_{jk}^{-1}$. As $\mathcal{C}_i^{(0)}$ are independent of the renormalization scale μ , Eq. (3.7) leads to the running of the renormalized Wilson coefficients in terms of the anomalous dimension matrix (ADM) [93, 94], defined to be γ , as

$$\mu \frac{d\mathcal{C}_i(\mu)}{d\mu} = (\gamma^T)_{ij} \mathcal{C}_j(\mu) , \quad \gamma \equiv \mathcal{Z}^{-1} \mu \frac{d\mathcal{Z}}{d\mu} , \quad (3.9)$$

where the elements in i th column of γ gives the RGE for \mathcal{C}_i .

In $\overline{\text{MS}}$, one can now expand these matrices in orders of $1/\epsilon$ poles as

$$\begin{aligned} \mathcal{Z} &= I + \frac{1}{\epsilon} \mathcal{Z}_{(1)}(\alpha_s, \alpha_w, \alpha_t) + \frac{1}{\epsilon^2} \mathcal{Z}_{(2)}(\alpha_s, \alpha_w, \alpha_t) + \dots , \\ \mathcal{R} &= I + \frac{1}{\epsilon} \mathcal{R}_{(1)}(\alpha_s, \alpha_w, \alpha_t) + \frac{1}{\epsilon^2} \mathcal{R}_{(2)}(\alpha_s, \alpha_w, \alpha_t) + \dots , \\ \chi &= I + \frac{1}{\epsilon} \chi_{(1)}(\alpha_s, \alpha_w, \alpha_t) + \frac{1}{\epsilon^2} \chi_{(2)}(\alpha_s, \alpha_w, \alpha_t) + \dots , \end{aligned} \quad (3.10)$$

where, $\mathcal{Z}_{(1)}$ represents the co-efficient of $1/\epsilon$ poles and so on. It is now straightforward to show that $\gamma(\alpha_s, \alpha_w, \alpha_t)$ only depends on the $1/\epsilon$ pole pieces

$$\gamma(\alpha_s, \alpha_w, \alpha_t) = -2\alpha_s \frac{\partial \mathcal{Z}_{(1)}}{\partial \alpha_s} - 2\alpha_w \frac{\partial \mathcal{Z}_{(1)}}{\partial \alpha_w} - 2\alpha_t \frac{\partial \mathcal{Z}_{(1)}}{\partial \alpha_t} , \quad (3.11)$$

where α_s, α_w are the coupling constants for the strong and weak force while α_t is related to top Yukawa coupling: $\alpha_t \equiv y_t^2/4\pi$.

As $\mathcal{Z} = \mathcal{R}\chi$, this readily implies $\mathcal{Z}_{(1)} = \mathcal{R}_{(1)} + \chi_{(1)}$. Therefore, we only require the $1/\epsilon$ poles of the wavefunction renormalization and the full renormalization diagrams to compute γ . Expanding the relevant matrices, i.e., $\mathcal{R}_{(1)}, \chi_{(1)}$ and γ order-by-order in the strong and electroweak gauge couplings and the Yukawa coupling, we obtain

$$\begin{aligned} \mathcal{R}_{(1)} &= \frac{\alpha_s}{4\pi} \mathcal{A}_s + \frac{\alpha_w}{16\pi} \mathcal{A}_w + \frac{\alpha_t}{16\pi} \mathcal{A}_t + \frac{\alpha_s \alpha_w}{64\pi^2} \mathcal{A}_{sw} + \dots , \\ \chi_{(1)} &= \frac{\alpha_s}{4\pi} \mathcal{B}_s + \frac{\alpha_w}{16\pi} \mathcal{B}_w + \frac{\alpha_t}{16\pi} \mathcal{B}_t + \frac{\alpha_s \alpha_w}{64\pi^2} \mathcal{B}_{sw} + \dots , \\ \gamma &= \frac{\alpha_s}{4\pi} \gamma_s + \frac{\alpha_w}{16\pi} \gamma_w + \frac{\alpha_t}{16\pi} \gamma_t + \frac{\alpha_s \alpha_w}{64\pi^2} \gamma_{sw} + \dots , \end{aligned} \quad (3.12)$$

where, evidently [93]

$$\begin{aligned} \gamma_s &= -2(\mathcal{A}_s + \mathcal{B}_s) , & \gamma_w &= -2(\mathcal{A}_w + \mathcal{B}_w) , \\ \gamma_t &= -2(\mathcal{A}_t + \mathcal{B}_t) , & \gamma_{sw} &= -4(\mathcal{A}_{sw} + \mathcal{B}_{sw}) . \end{aligned} \quad (3.13)$$

The elements $\mathcal{A}(i, j)$ at a given coupling order are derived from the self-energy diagrams at that order which renormalize the SM fields of \mathcal{O}_i , changing it to \mathcal{O}_j . In contrast, the elements of $\mathcal{B}(i, j)$ are obtained from diagrams generating operator \mathcal{O}_j by insertion of operator \mathcal{O}_i , where i can also be the same as j . Finally, Eq. (3.13) gives the anomalous dimension matrix of that particular order.

We provide the general structure of the field strength renormalization and full renormalization matrices obtained in this work in a compact form using flavor indices i, j .

	aGG	$a\bar{u}_{L,j}u_{L,j}$	$a\bar{u}_{R,j}u_{R,j}$	$a\bar{d}_{L,j}d_{L,j}$	$a\bar{d}_{R,j}d_{R,j}$	$a\bar{s}_Lb_L$
$aG^{(0)}G^{(0)}$	$\mathcal{A}_s(1, 1)$	0	0	0	0	0
$a\bar{u}_{L,i}^{(0)}u_{L,i}^{(0)}$	0	$\mathcal{A}_{(s+w+t)}(2L, 2L)_{ij}$	0	0	0	0
$a\bar{u}_{R,i}^{(0)}u_{R,i}^{(0)}$	0	0	$\mathcal{A}_{(s+w+t)}(2R, 2R)_{ij}$	0	0	0
$a\bar{d}_{L,i}^{(0)}d_{L,i}^{(0)}$	0	0	0	$\mathcal{A}_{(s+w)}(3L, 3L)_{ij}$	0	$\mathcal{A}_w(3L, 4L)_i$
$a\bar{d}_{R,i}^{(0)}d_{R,i}^{(0)}$	0	0	0	0	$\mathcal{A}_{(s+w)}(3R, 3R)_{ij}$	0
$a\bar{s}_L^{(0)}b_L^{(0)}$	0	0	0	$\mathcal{A}_w(4L, 3L)_j$	0	$\mathcal{A}_{(s+w)}(4L, 4L)$

Table 1. Structure of the wavefunction renormalization matrix. Subscripts s and w denote renormalization at the $\mathcal{O}(\alpha_s)$ and $\mathcal{O}(\alpha_w)$ via the gluon and electroweak gauge boson loop, respectively. While subscript t denotes the top-Yukawa contribution. The off-diagonal entries appear because of quark-mixing via W -boson exchange. We ignore any electromagnetic contribution in our analysis.

	$\langle\mathcal{O}_1\rangle^{tree}$	$\langle\mathcal{O}_{2L}^j\rangle^{tree}$	$\langle\mathcal{O}_{2R}^j\rangle^{tree}$	$\langle\mathcal{O}_{3L}^j\rangle^{tree}$	$\langle\mathcal{O}_{3R}^j\rangle^{tree}$	$\langle\mathcal{O}_{4L}\rangle^{tree}$
$\langle\mathcal{O}_1\rangle^{(0)}$	$\mathcal{B}_s(1, 1)$	$\mathcal{B}_s(1, 2L)_j$	$\mathcal{B}_s(1, 2R)_j$	$\mathcal{B}_s(1, 3L)_j$	$\mathcal{B}_s(1, 3R)_j$	$\mathcal{B}_{sw}(1, 4L)$
$\langle\mathcal{O}_{2L}^i\rangle^{(0)}$	0	$\mathcal{B}_w(2L, 2L)_{ij}$	$\mathcal{B}_{(w+t)}(2L, 2R)_{ij}$	$\mathcal{B}_w(2L, 3L)_{ij}$	0	$\mathcal{B}_w(2L, 4L)_i$
$\langle\mathcal{O}_{2R}^i\rangle^{(0)}$	0	$\mathcal{B}_{(w+t)}(2R, 2L)_{ij}$	$\mathcal{B}_w(2R, 2R)_{ij}$	$\mathcal{B}_w(2R, 3L)_{ij}$	0	$\mathcal{B}_w(2R, 4L)_i$
$\langle\mathcal{O}_{3L}^i\rangle^{(0)}$	0	$\mathcal{B}_w(3L, 2L)_{ij}$	$\mathcal{B}_w(3L, 2R)_{ij}$	$\mathcal{B}_w(3L, 3L)_{ij}$	$\mathcal{B}_w(3L, 3R)_{ij}$	0
$\langle\mathcal{O}_{3R}^i\rangle^{(0)}$	0	0	0	$\mathcal{B}_w(3R, 3L)_{ij}$	$\mathcal{B}_w(3R, 2R)_{ij}$	0
$\langle\mathcal{O}_{4L}\rangle^{(0)}$	0	$\mathcal{B}_w(4L, 2L)_j$	$\mathcal{B}_w(4L, 2R)_j$	$\mathcal{B}_w(4L, 3L)_j$	0	$\mathcal{B}_w(4L, 4L)$

Table 2. Structure of the full renormalization matrix. We follow the same notation for the subscript and the indices as explained before. The two-loop contribution to $b \rightarrow sa$ is boxed.

In Table 1, we write down the wavefunction renormalization of our composite operators Eq.(2.2), whereas in Table 2, we provide the complete renormalization matrix. The subscripts s, w and t represent renormalization at the α_s, α_w and α_t order, respectively. For example, \mathcal{B}_{sw} represents full renormalization at the order $\alpha_s\alpha_w$. This particular entry encapsulates the contribution to the $b - s - a$ operator, from the prototypical $a - G - \tilde{G}$ operator. The leading order effect arises at the two-loop level, explaining the order of α . In addition, in both tables, depending on the particular operator structure, the indices i, j represent the flavor of the up-/down-type quarks. The entries without any index represent a single element. Those with one index are column or row matrices containing three elements, while those with both i, j indices are 3×3 matrices containing 9 elements.

3.2 Anomalous dimension matrix

To determine the dominant contributions to the anomalous dimension matrix, we adhere to the following schemes:

1. **Naive Dimensional Regularization:** Throughout the paper, we work in the Feynman gauge and employ the widely used naive dimensional regularization [95] in $d = 4 - 2\epsilon$ dimensions to regulate the UV divergences. We also use d -dimensional Dirac algebra for all γ^μ matrices, i.e.,

$$\{\gamma_\mu, \gamma_\nu\} = 2g_{\mu\nu}, \quad \text{and} \quad \{\gamma_\mu, \gamma_5\} = 0. \quad (3.14)$$

Furthermore, explicit relations between the ϵ tensor and γ_5 are used only when all UV divergences are evaluated in terms of $1/\epsilon$ poles and we return to $d = 4$. We note in passing that Eq. (3.14) is valid as long as we are not dealing with any closed-parity fermion loop. Such diagrams are usually finite and do not affect the determination of the anomalous dimension matrix. A more rigorous treatment, involving the 't Hooft-Veltman scheme [96], will be addressed in future work [97].

2. We consider the limit in which all external momenta and light-quark masses are set to zero. This approximation induces infrared divergences, which we regulate separately. We also expand about the axion momenta $\ell = 0$ and take only the leading non-vanishing terms in all diagrams. We have checked that the inclusion of non-zero quark masses introduces a correction of order $(m_b/M_W)^2$. Additionally, our approximation simplifies the analysis by avoiding complexities associated with two-loop master integrals in the presence of nonvanishing external momentum.
3. **NDR with mass regularization:** To regularize the IR divergences in scaleless integrals or otherwise, we use a fictitious IR mass m_R for the gluon and light quark propagators (b and s) within the loop diagrams. As a result, we make the following substitutions to the propagators:

$$\frac{-ig_{\mu\nu}}{\tilde{q}^2} \rightarrow \frac{-ig_{\mu\nu}}{\tilde{q}^2 - m_R^2}, \quad \frac{\tilde{k}}{\tilde{k}^2} \rightarrow \frac{\tilde{k}}{\tilde{k}^2 - m_R^2}, \quad (3.15)$$

where \tilde{q} or \tilde{k} are generic and can include other external momenta, including the loop momenta k or q . We also did not put any IR mass in the numerator to simplify the light-quark propagators. The inclusion of such terms might generate spurious or evanescent chirality flip operators in some of the two-loop diagrams and their associated counterterms. Choices for other infrared (IR) regulators, such as the assignment of nonzero off-shell momenta to the external legs, may also be considered. However, these approaches can result in non-trivial master integrals.

4. Renormalization of composite operators deals with matrix elements which are amputated Green's functions [92, 93, 98]. As a result, our analysis requires only one-part irreducible (1PI) diagrams to be considered.

We will now proceed with the calculation of different elements in the ADM, i.e. \mathcal{A} and \mathcal{B} elements at each order.

3.2.1 $\mathcal{O}(\alpha_s)$

\mathcal{A}_s elements: At $\mathcal{O}(\alpha_s)$ order, the wave function renormalization for the SM gluon and quark fields are well established and given by

$$\mathcal{R}_{gg} = 1 + \frac{\alpha_s}{4\pi\epsilon}(\beta_0 - 2C_A), \quad \mathcal{R}_{qq} = 1 - \frac{\alpha_s C_F}{4\pi\epsilon}, \quad (3.16)$$

where $\beta_0 = 11C_A/3 - 2N_f/3$ and $N_f = 6$ are the number of quark flavors and $C_A = 3, C_F = 4/3$, are the quadratic Casimirs. The gluon wavefunction renormalization matrix element is defined by \mathcal{R}_{gg} as $\mathcal{A}_s(1, 1) = \beta_0 - 2C_A$ as the $a - G - \tilde{G}$ operator is quadratic in the gluon field and similarly for the quark fields. We note that the gluon and quark wave functions do not mix under field renormalization, resulting in all other entries in the first row and column of Table 1 being zero at any order in the couplings. The renormalization of the quark field \mathcal{R}_{qq} in $\mathcal{O}(\alpha_s)$ contributes uniformly to all other diagonal entries in \mathcal{A}_s , since it is independent of the handedness, flavor, or charge of the quark. Moreover, each diagonal entry itself is diagonal as there is no mixing between different flavors of the same handedness or charge. Therefore, all non-diagonal entries of \mathcal{A}_s are zero and the diagonal entries are:

$$\begin{aligned} \mathcal{A}_s(1, 1) &= \beta_0 - 2C_A, \\ \mathcal{A}_s(2L, 2L) &= \mathcal{A}_s(2R, 2R) = \mathcal{A}_s(3L, 3L) = \mathcal{A}_s(3R, 3R) = -C_F\delta_{ij}, \\ \mathcal{A}_s(4L, 4L) &= -C_F. \end{aligned} \quad (3.17)$$

\mathcal{B}_s elements: To determine the \mathcal{B}_s entries, we evaluate diagrams where the operator \mathcal{O}_j is generated by inserting the operator \mathcal{O}_i with a gluon loop. We reiterate that i can also be equal to j . At $\mathcal{O}(\alpha_s)$, the following elements are of particular interest. For example, $\mathcal{B}_s(1, 1)$ represents the pole structure associated with the generation of the operator \mathcal{O}_1 due to the insertion of the same operator, as illustrated in Fig. 2. At $\mathcal{O}(\alpha_s)$, axion-fermion insertions of $\mathcal{O}_{2L/R}, \mathcal{O}_{3L/R}, \mathcal{O}_{4L}$ can also generate \mathcal{O}_1 . However, such diagrams involve triangle fermionic loops, which are finite. Consequently, these diagrams do not contribute to the entries of \mathcal{B}_s . Therefore, it follows that the other entries in the first column of \mathcal{B}_s are zero.

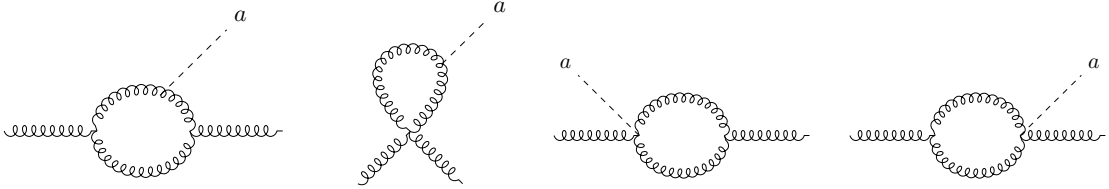


Figure 2. The diagrams contributing to $\mathcal{B}_s(1, 1)$. The dashed line represents the axion. The Lorentz and color indices of gluons are not shown explicitly since the operator structure does not enter in the elements of the ADM.

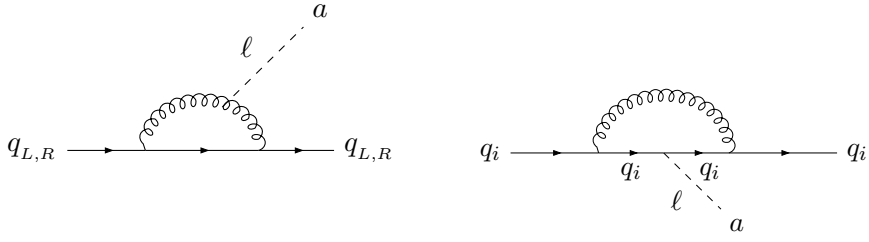


Figure 3. Left panel: Diagram for the first row entries: $\mathcal{B}_s(1, 2L/R)$ and $\mathcal{B}_s(1, 3L/R)$. Right panel: Diagram for evaluating diagonal entries of \mathcal{B}_s .

On the other hand, \mathcal{O}_1 insertion generates all axion-quark diagonal operators at $\mathcal{O}(\alpha_s)$ via the type of diagram shown to the left of Fig. 3, thereby giving rise to nonzero first row entries except $\mathcal{B}_s(1, 4L)$ which requires a flavor change. We note that the Dirac structure of the left- and right-handed fermion-axion interaction operators of our Lagrangian is $(-\not{\ell}P_L)$ and $(-\not{\ell}P_R)$ (see Appendix A). This leads to a relative sign difference in these elements when a diagram result shows in terms of a $\not{\ell}\gamma_5$ Dirac structure. Finally, diagonal axion-fermion operators arise from the insertion of the same operators as depicted in the right panel of Fig. 3.

These exhaust all non-zero contributions to \mathcal{B}_s . We find

$$\begin{aligned}
 \mathcal{B}_s(1, 1) &= 2C_A, \\
 \mathcal{B}_s(2L, 2L) &= \mathcal{B}_s(2R, 2R) = \mathcal{B}_s(3L, 3L) = \mathcal{B}_s(3R, 3R) = C_F\delta_{ij}, \mathcal{B}_s(4L, 4L) = C_F, \\
 \mathcal{B}_s(1, 2L) &= \mathcal{B}_s(1, 3L) = -\mathcal{B}_s(1, 2R) = -\mathcal{B}_s(1, 3R) = 6C_F.
 \end{aligned} \tag{3.18}$$

The entries in the last line above are 1×3 matrices, with all elements equal to $6C_F$. Recall that, at the $\mathcal{O}(\alpha_s)$ order, the anomalous dimension matrix is defined to be $\gamma_s = -2(\mathcal{A}_s + \mathcal{B}_s)$, which we obtain using Eq. (3.17), (3.18) as

$$\gamma_s = \begin{pmatrix} -2\beta_0 & -12C_F & 12C_F & -12C_F & 12C_F & 0 \\ 0 & 0 & 0 & 0 & 0 & 0 \\ 0 & 0 & 0 & 0 & 0 & 0 \\ 0 & 0 & 0 & 0 & 0 & 0 \\ 0 & 0 & 0 & 0 & 0 & 0 \end{pmatrix}. \tag{3.19}$$

We see that all Wilson coefficients receive their leading order RGE contribution at $\mathcal{O}(\alpha_s)$, except the last one, i.e., \mathcal{C}_{4L} . We will show that the leading-order contribution for the running of \mathcal{C}_{4L} appears at $\mathcal{O}(\alpha_w)$ and $\mathcal{O}(\alpha_s\alpha_w)$.

3.2.2 $\mathcal{O}(\alpha_w)$

\mathcal{A}_w elements: The gluon field doesn't mix with itself and the quark field at this order (i.e. via weak interaction), so the first row and column have all elements equal to zero. However, the renormalization of the wave function of quark operators receives diagonal contributions from the W and Z quark self-energy graphs, as shown in Fig. 4. The resulting

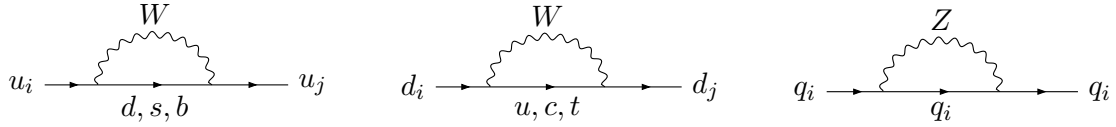


Figure 4. Diagrams contributing to fermionic diagonal elements of \mathcal{A}_w . We work in the Feynman gauge, where Goldstone loops of W and Z denoted by W_G and Z_G are also considered. We do not label them explicitly in the diagrams. The left and middle diagrams can change quark flavor.

renormalizations from the left and middle diagrams of Fig. 4 are

$$\begin{aligned}
[\mathcal{R}_{u,L}]_{ii}(W) &= 1 + \frac{\alpha_w}{16\pi\epsilon} \left[- \sum_{k=d,s,b} 2|V_{ik}|^2 \right], \\
[\mathcal{R}_{u,R}]_{ij}(W_G) &= 1 + \frac{\alpha_w}{16\pi\epsilon} \left[- \sum_{k=d,s,b} V_{jk}^* V_{ik} \sqrt{\xi_i \xi_j} \right], \\
[\mathcal{R}_{d,L}]_{ij}(W + W_G) &= 1 + \frac{\alpha_w}{16\pi\epsilon} \left[- \sum_{k=u,c,t} 2|V_{ki}|^2 \delta_{ij} - \sum_{k=u,c,t} V_{kj}^* V_{ki} \xi_k \right], \quad (3.20)
\end{aligned}$$

and for the rightmost diagram of Fig. 4

$$\mathcal{R}_q(Z + Z_G) = 1 + \frac{\alpha_w}{16\pi\epsilon} \left[- \left(\frac{c_{L/R}^q}{c_w} \right)^2 - \frac{\xi_q}{2} \right], \quad (3.21)$$

for any up or down type quark q and handedness L/R . Here, V_{ki} 's are the CKM matrix element, $\xi_i \equiv m_i^2/M_W^2$ and $c_w = \cos\theta_w$ with θ_w the weak mixing angle. $c_{L/R}^q$ are the usual Z boson couplings with the left- and right-handed quarks. However, they do not appear in the RGEs, as they cancel out after adding the full renormalization while calculating the ADM. These renormalizations contribute to the 5 diagonal entries of \mathcal{A}_w .

Furthermore, two non-diagonal entries in \mathcal{A}_w come from the FCNC self-energy loops shown in Fig. 5.

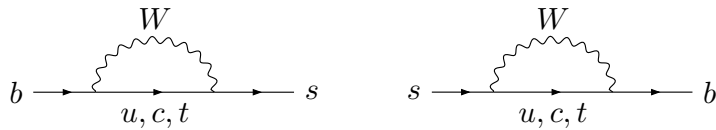


Figure 5. Left: FCNC diagram contributing to non-zero off-diagonal entry $\mathcal{A}_w(3L, 4L)$. Right: The same diagram with initial and final states interchanged contributes to $\mathcal{A}_w(4L, 3L)$.

The left and right panel diagrams give the following flavor-changing field renormalizations, respectively

$$\begin{aligned}
[\mathcal{R}_{d,L}]_{bs}(W + W_G) &= - \frac{\alpha_w}{16\pi\epsilon} \left[\sum_{k=u,c,t} V_{ks}^* V_{kb} \xi_k \right], \\
[\mathcal{R}_{d,L}]_{sb}(W + W_G) &= - \frac{\alpha_w}{16\pi\epsilon} \left[\sum_{k=u,c,t} V_{kb}^* V_{ks} \xi_k \right]. \quad (3.22)
\end{aligned}$$

In particular, the quark operators \mathcal{O}_{3L}^s and \mathcal{O}_{3L}^b are renormalized to \mathcal{O}_{4L} . One of the quark fields changes flavor Eq. (3.22), and the other one is renormalized diagonally Eq. (3.20), (3.21). This is why \mathcal{O}_{3L}^d does not get renormalized to \mathcal{O}_{4L} at $\mathcal{O}(\alpha_w)$, since both the d quark fields in the operator would have to change flavor, which makes the renormalization of $\mathcal{O}(\alpha_w^2)$ order.

The field renormalization matrix at $\mathcal{O}(\alpha_w)$ thus contains the following non-zero entries

$$\begin{aligned}
\mathcal{A}_w(2L, 2L) &= \left[- \left(\frac{(c_L^u)^2}{c_w^2} + \frac{\xi_i}{2} \right) - 2 \sum_{k=d,s,b} |V_{ik}|^2 \right] \delta_{ij} , \\
\mathcal{A}_w(2R, 2R) &= - \left[\frac{(c_R^u)^2}{c_w^2} + \frac{\xi_i}{2} \right] \delta_{ij} - \sum_{k=d,s,b} V_{jk}^* V_{ik} \sqrt{\xi_i \xi_j} , \\
\mathcal{A}_w(3L, 3L) &= \left[- \left(\frac{(c_L^d)^2}{c_w^2} + \frac{\xi_i}{2} \right) - 2 \sum_{k=u,c,t} |V_{ki}|^2 \right] \delta_{ij} - \sum_{k=u,c,t} (V_{kj}^* V_{ki} \xi_k) , \\
\mathcal{A}_w(3R, 3R) &= - \left[\frac{(c_R^d)^2}{c_w^2} + \frac{\xi_i}{2} \right] \delta_{ij} , \\
\mathcal{A}_w(4L, 4L) &= - \left(\frac{(c_L^d)^2}{c_w^2} + \frac{\xi_s + \xi_b}{2} \right) - \frac{1}{2} \left[\sum_{k=u,c,t} |V_{ks}|^2 (2 + \xi_k) + \sum_{k=u,c,t} |V_{kb}|^2 (2 + \xi_k) \right] , \\
\mathcal{A}_w(3L, 4L) &= \left[- \frac{1}{2} \sum_{k=u,c,t} (V_{ks}^* V_{kb} \xi_k) \right] (1 - \delta_{id}) , \\
\mathcal{A}_w(4L, 3L) &= \left[- \frac{1}{2} \sum_{k=u,c,t} (V_{ks}^* V_{kb} \xi_k) \right] (1 - \delta_{jd}) . \tag{3.23}
\end{aligned}$$

\mathcal{B}_w elements: At the $\mathcal{O}(\alpha_w)$ order, the full renormalization introduces diagonal and off-diagonal entries. In particular, there is a generation of the operator \mathcal{O}_{4L} from the insertion of $\mathcal{O}_{2L}, \mathcal{O}_{2R}$. These operator insertions also generate $\mathcal{O}_{2L/R}$ and \mathcal{O}_{3L} through the W, Z loops (see to the left of Fig. 6).

Left- and right-handed axion-down-type quark operators generate different operators through RGEs. For example, insertion of \mathcal{O}_{3L} generates $\mathcal{O}_{2L/R}$ and $\mathcal{O}_{3L/R}$ while inserting \mathcal{O}_{3R} generates only $\mathcal{O}_{3L/R}$ because in this case the W and W_G loops are finite. Finally, the insertion of \mathcal{O}_{4L} generates $\mathcal{O}_{2L/R}$ through W and W_G while \mathcal{O}_{4L} itself is generated from a Z boson loop. The Goldstone result Z_G is proportional to $m_s m_b / M_W^2 \approx 0$ and is neglected.

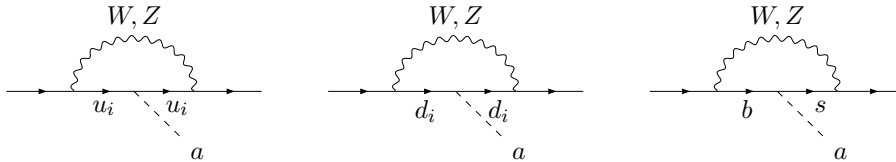


Figure 6. Operator insertion diagrams for \mathcal{B}_w entries. The leftmost diagram is the insertion of $\mathcal{O}_{2L/R}$ in W and Z loops (along with their Goldstones). Explicit final quark states decide which operator is being generated. They depend on the insertion and the boson. The middle diagram shows the insertion of $\mathcal{O}_{3L/R}$, i.e., the down-type axion quark flavor diagonal operators. The rightmost diagram is the insertion of flavor off-diagonal \mathcal{O}_{4L} .

We thus obtain the full renormalization matrix at $\mathcal{O}(\alpha_w)$ with the following non-zero entries

$$\begin{aligned}
\mathcal{B}_w(4L, 4L) &= \frac{(c_L^d)^2}{c_w^2}, \\
\mathcal{B}_w(2L, 2L) &= \frac{(c_L^u)^2}{c_w^2} \delta_{ij}, \quad \mathcal{B}_w(2R, 2R) = \frac{(c_R^u)^2}{c_w^2} \delta_{ij}, \\
\mathcal{B}_w(3L, 3L) &= \frac{(c_L^d)^2}{c_w^2} \delta_{ij}, \quad \mathcal{B}_w(3R, 3R) = \frac{(c_R^d)^2}{c_w^2} \delta_{ij}, \\
\mathcal{B}_w(2L, 2R) &= \frac{\xi_i}{2} \delta_{ij}, \quad \mathcal{B}_w(2L, 3L) = 2|V_{ij}|^2, \quad \mathcal{B}_w(2L, 4L) = 2(V_{is}^* V_{ib}), \\
\mathcal{B}_w(2R, 2L) &= \frac{\xi_i}{2} \delta_{ij}, \quad \mathcal{B}_w(2R, 3L) = |V_{ij}|^2 \xi_i, \quad \mathcal{B}_w(2R, 4L) = (V_{is}^* V_{ib} \xi_i), \\
\mathcal{B}_w(3L, 2L) &= 2|V_{ji}|^2, \quad \mathcal{B}_w(3L, 2R) = |V_{ji}|^2 \xi_j, \quad \mathcal{B}_w(3L, 3R) = \frac{\xi_i}{2} \delta_{ij}, \\
\mathcal{B}_w(3R, 3L) &= \frac{\xi_i}{2} \delta_{ij}, \\
\mathcal{B}_w(4L, 2L) &= 2V_{js}^* V_{jb}, \quad \mathcal{B}_w(4L, 2R) = (V_{js}^* V_{jb} \xi_j). \tag{3.24}
\end{aligned}$$

The matrix γ_w can now be obtained from Eq. (3.23), (3.24), and Eq. (3.13). We consider the following simplifications.

- $\xi_i \approx 0$ for $i = d, s, b, u, c$
- CKM elements are taken non-zero up to $\mathcal{O}(\lambda^2)$ in the Wolfenstein parameterization.
- CKM unitarity is used for summations: $\sum_k |V_{ki}|^2 = 1$ for any i . In cases of ξ_k appearing with the summation, the first point implies: $\sum_{k=d,s,b} V_{ik}^* V_{jk} \xi_k \approx 0$ while $\sum_{k=u,c,t} V_{ki}^* V_{kj} \xi_k \approx V_{ti}^* V_{tj} \xi_t$.

Implementing these, we find

$$\gamma_w = \begin{pmatrix} 0 & 0 & 0 & 0 & 0 & 0 \\ 0 & (4 + \xi_i) \delta_{ij} & -\xi_i \delta_{ij} & -4|V_{ij}|^2 & 0 & -4(V_{is}^* V_{ib}) \\ 0 & -\xi_i \delta_{ij} & \xi_i \delta_{ij} + 2\xi_t |V_{tb}|^2 \delta_{it} \delta_{jt} & -2|V_{ij}|^2 \xi_i & 0 & -2(V_{is}^* V_{ib} \xi_i) \\ 0 & -4|V_{ji}|^2 & -2|V_{ji}|^2 \xi_j & 4\delta_{ij} + 2V_{tj}^* V_{ti} \xi_t & 0 & (1 - \delta_{id})(V_{ts}^* V_{tb} \xi_t) \\ 0 & 0 & 0 & 0 & 0 & 0 \\ 0 & -4V_{js}^* V_{jb} & -2(V_{js}^* V_{jb} \xi_j) & (1 - \delta_{dj})(V_{ts}^* V_{tb} \xi_t) & 0 & 4 + |V_{tb}|^2 \xi_t \end{pmatrix} \tag{3.25}$$

3.2.3 $\mathcal{O}(\alpha_t)$

Here, the top Yukawa contribution is the only relevant contribution compared to the other flavors because $y_t = \sqrt{2}m_t/v \approx 1$, where v is the electroweak symmetry breaking scale.

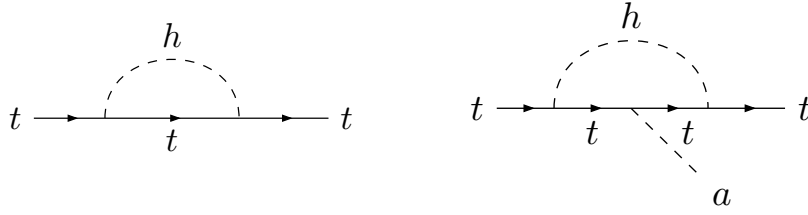


Figure 7. The self-energy diagram for $A_t(2L, 2L)$ and $A_t(2R, 2R)$, and $\mathcal{O}_{2L,2R}^t$ operator inserted diagram for $\mathcal{B}_t(2L, 2R)$ and $\mathcal{B}_t(2R, 2L)$.

\mathcal{A}_t elements: The Yukawa contribution to the wave-function renormalization of top-quark is (see Fig. 7 left-panel)

$$\mathcal{R}_{tt} = 1 - \frac{y_t^2}{64\pi^2} \frac{1}{\epsilon} = 1 - \frac{\alpha_t}{16\pi\epsilon} . \quad (3.26)$$

This gives the following non-zero \mathcal{A}_t entries:

$$\mathcal{A}_t(2L, 2L) = \mathcal{A}_t(2R, 2R) = -\delta_{it}\delta_{jt} . \quad (3.27)$$

\mathcal{B}_t elements: The insertion of \mathcal{O}_{2L}^t and \mathcal{O}_{2R}^t (Fig. 7 right-panel) gives the full renormalization \mathcal{B}_t entries:

$$\mathcal{B}_t(2L, 2R) = \mathcal{B}_t(2R, 2L) = \delta_{it}\delta_{jt} . \quad (3.28)$$

Here i, j are different up-type quark fields. From these, we obtain γ_t :

$$\gamma_t = \begin{pmatrix} 0 & 0 & 0 & 0 & 0 & 0 \\ 0 & 2\delta_{it}\delta_{jt} & -2\delta_{it}\delta_{jt} & 0 & 0 & 0 \\ 0 & -2\delta_{it}\delta_{jt} & 2\delta_{it}\delta_{jt} & 0 & 0 & 0 \\ 0 & 0 & 0 & 0 & 0 & 0 \\ 0 & 0 & 0 & 0 & 0 & 0 \\ 0 & 0 & 0 & 0 & 0 & 0 \end{pmatrix} . \quad (3.29)$$

3.2.4 $\mathcal{O}(\alpha_s\alpha_w)$

A significant contribution to \mathcal{C}_{4L} from \mathcal{C}_1 arises at the two-loop order, specifically $\mathcal{O}(\alpha_s\alpha_w)$. This is crucial since the leading-order effect pertaining to the $b \rightarrow s$ transition is generated only at the two-loop level for heavy QCD axion and KSVZ-like scenarios. Given this, we focus our analysis on computing the $\mathcal{A}_{sw}(1, 4L)$ and $\mathcal{B}_{sw}(1, 4L)$ entries. Other coefficients have already accounted for the contributions from \mathcal{C}_1 to their running.

\mathcal{A}_{sw} elements: Self-energy corrections by definition do not mix quark and gluon fields; therefore $\mathcal{A}_{sw}(1, 4L)$ is zero.

\mathcal{B}_{sw} elements: On the other hand, the operator renormalization gets a non-zero contribution from the following diagrams, Fig. 8 where \mathcal{O}_1 generates \mathcal{O}_{4L} . We reiterate that for the computation of amputated Green's functions, loops on the external legs have not been considered.

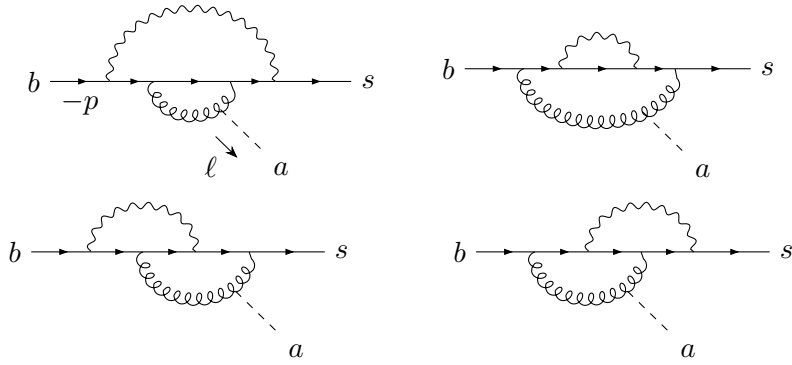


Figure 8. All possible two-loop 1PI diagrams relevant for the process $b \rightarrow sa$.

To evaluate the two-loop diagrams shown in Fig. 8, we use the following procedures.

1. In principle, the diagrams shown in Fig. 8 exhibit both ultraviolet (UV) and infrared (IR) divergences. To correctly determine the anomalous dimension, it is essential to distinguish between these divergent structures. Explicit calculations have confirmed that both the gluon subdiagram and the light-quark propagators are IR divergent. Consequently, we introduce a fictitious IR regulator, m_R , to address divergences in both the gluon and light quark fields.
2. We expand the axion momentum about $\ell = 0$ in the denominator. However, we keep the terms proportional only to $\not{\ell}$ in the numerator after the Dirac algebra. This is reasonable as we ignore m_a compared to other scales in the theory.
3. As mentioned earlier, we work in the limit where all the external momenta, i.e. $p = 0$. This helps us to simplify Feynman integrals as well as the corresponding master integrals. For the tensor reduction of the numerator, we have used FORM [99] whereas integration by parts was performed using KIRA [100]. We provide a detailed sample of a two-loop computation in Appendix B.

The divergent parts of the two-loop amplitudes for individual diagrams shown in Fig. 8 are given by

$$\begin{aligned}
i\Sigma_1 &= \kappa \left[-\frac{\xi}{2\epsilon^2} + \frac{1}{\epsilon} \left\{ -\xi \log \left(\frac{\mu^2}{M_W^2} \right) + \frac{\xi(5\xi - 17)}{4(\xi - 1)} + \frac{(\xi - 4)(\xi - 2)\xi \log \xi}{(\xi - 1)^2} \right\} \right] (-\not{\ell}P_L), \\
i\Sigma_{2,3} &= \kappa \left[\frac{\xi}{2\epsilon^2} + \frac{\xi}{\epsilon} \log \left(\frac{\mu^2}{m_R^2} \right) - \frac{3\xi}{4\epsilon} \right] (-\not{\ell}P_L), \\
i\Sigma_4 &= \kappa \left[-\frac{\xi}{2\epsilon^2} - \frac{\xi}{\epsilon} \log \left(\frac{\mu^2}{m_R^2} \right) + \frac{\xi}{12\epsilon} \right] (-\not{\ell}P_L),
\end{aligned} \tag{3.30}$$

where we define

$$\kappa \equiv 6 \left(\frac{\alpha_s}{4\pi} \right) \left(\frac{\alpha_w}{16\pi} \right) \left(\frac{C_1}{f_a} \right) C_F \delta_{ij} \sum_u V_{su}^* V_{ub}. \tag{3.31}$$

3.3 Counterterms

Note that the first diagram does not exhibit any IR poles. This is because the subdiagram with the gluon loop has a scale from the top-quark propagator. In the rest of the two-loop diagrams, the presence of light quarks associated with the gluon loop generates this IR divergence. In addition, we used CKM unitarity relations to evaluate these amplitudes. The divergences need to be canceled to make the theory renormalized at the UV scale itself. This requires the introduction of counterterms that can be identified from the divergent subdiagrams in Fig. 8. Some of these counterterms are already present in the SM, for example, the $b - s$ mixing and the $b - s - g$ operator generated via the W -boson loop. In addition, we require an additional operator that involves the interaction between the axion and diagonal quark fields. This has already been taken into account in our effective Lagrangian, given in Eq. (2.1). We illustrate these operators in Fig. 9, where the colored

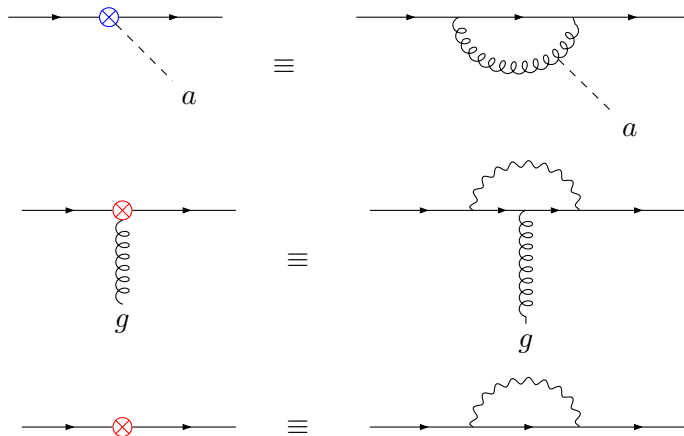


Figure 9. The colored crosses indicate $1/\epsilon$ pieces from the diagrams on the right.

crosses indicate $1/\epsilon$ pieces with appropriate coefficients, which are generated from the one-loop diagrams on the right. Once the counterterms are identified, they are plugged into the counterdiagrams shown in Fig. 10. We emphasize that in the $\overline{\text{MS}}$ scheme, only $1/\epsilon$ pieces of these diagrams are considered for the counterterm insertion. The amplitudes from the

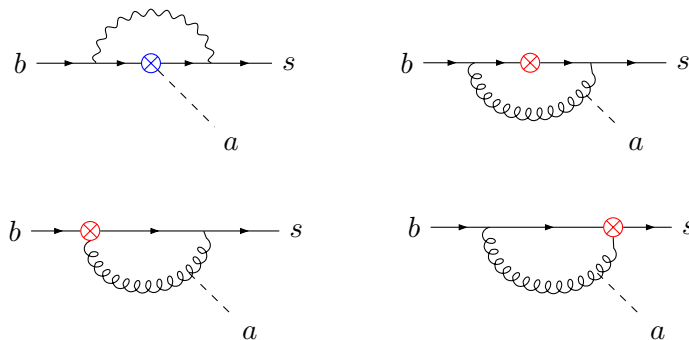


Figure 10. 1PI counter diagrams after incorporating the one-loop diagrams from Fig. 9

counter diagrams are obtained as

$$\begin{aligned}
i\Pi_1 &= \kappa \left[\frac{\xi}{\epsilon^2} + \frac{1}{\epsilon} \left\{ \xi \log \left(\frac{\mu^2}{M_W^2} \right) - \frac{(\xi^2 - 6\xi + 8) \xi \log \xi}{(\xi - 1)^2} - \frac{(\xi - 7)\xi}{2(\xi - 1)} \right\} \right] (-\not{P}_L), \\
i\Pi_{2,3} &= \kappa \left[-\frac{\xi}{\epsilon^2} - \frac{\xi}{\epsilon} \log \left(\frac{\mu^2}{m_R^2} \right) \right] (-\not{P}_L), \\
i\Pi_4 &= \kappa \left[\frac{\xi}{\epsilon^2} + \frac{1}{\epsilon} \left\{ -\frac{\xi}{3} + \xi \log \left(\frac{\mu^2}{m_R^2} \right) \right\} \right] (-\not{P}_L). \tag{3.32}
\end{aligned}$$

Notice that after including the amplitudes from the counter diagrams shown in Eq. (3.32), all the double UV poles, as well as UV-IR mixed poles, cancel from Eq. (3.30). However, we are still left with an overall $1/\epsilon$ pole, which necessitates the introduction of a different counterterm or operator of the form axion-quark off-diagonal interaction, i.e., $b - s - a$ operator, also included in Eq. (2.1) and shown in Fig. 11.

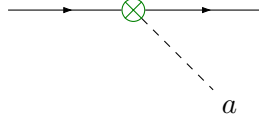


Figure 11. Overall counter term diagram, i.e., $b - s - a$ operator, which absorbs the remaining $1/\epsilon$ UV pole as presented in Eq. (3.33).

The corresponding amplitude for the overall counterterm for the operator $b - s - a$ is

$$i\Pi_{\text{Overall}} = - \left(\sum_{j=1}^4 i\Sigma_j + \sum_{j=1}^4 i\Pi_j \right) = \kappa \left[\frac{\xi}{\epsilon} \right] (-\not{P}_L). \tag{3.33}$$

This is also expected from the bottom-up approach of constructing an effective field theory since all possible operators are required to be written down in the Lagrangian to make the theory renormalizable order by order. Moreover, this remaining UV pole also contributes to \mathcal{B}_{sw} and eventually to the anomalous dimension matrix. We therefore get the following

$$\mathcal{B}_{sw}(1, 4L) = -6C_F(V_{ts}^* V_{tb} \xi_t), \tag{3.34}$$

which implies at $\mathcal{O}(\alpha_s \alpha_w)$ there is only one relevant non-zero entry in the ADM:

$$\gamma_{sw} = \begin{pmatrix} 0 & 0 & 0 & 0 & 0 & 24C_F(V_{ts}^* V_{tb} \xi_t) \\ 0 & 0 & 0 & 0 & 0 & 0 \\ 0 & 0 & 0 & 0 & 0 & 0 \\ 0 & 0 & 0 & 0 & 0 & 0 \\ 0 & 0 & 0 & 0 & 0 & 0 \\ 0 & 0 & 0 & 0 & 0 & 0 \end{pmatrix}. \tag{3.35}$$

This concludes the discussion about anomalous dimension matrix γ , which can be formed by adding Eqs. (3.19), (3.25), (3.29) and (3.35). There are subtleties involving the finite

terms that act as a matching coefficient for the overall Wilson coefficient at the M_W scale. We will discuss this in detail in the next section.

3.4 Complete set of RGEs

The two-loop anomalous dimension matrix for the analysis $b \rightarrow sa$ can now be translated to the running of Wilson coefficients, and we obtain ² using Eq. (3.9)

$$\begin{aligned}
\mu \frac{d\mathcal{C}_1}{d\mu} &= -\frac{\alpha_s \beta_0}{2\pi} \mathcal{C}_1, \\
\mu \frac{d\mathcal{C}_{2L}^j}{d\mu} &= -\frac{3\alpha_s C_F}{\pi} \mathcal{C}_1 + \frac{\alpha_w}{16\pi} \left(4\mathcal{C}_{2L}^j - 4 \sum_{i=d,s,b} |V_{ji}|^2 \mathcal{C}_{3L}^i - 4V_{js}^* V_{jb} \mathcal{C}_{4L} \right), \text{ for } j = (u, c), \\
\mu \frac{d\mathcal{C}_{2L}^t}{d\mu} &= -\frac{3\alpha_s C_F}{\pi} \mathcal{C}_1 + \frac{\alpha_t}{16\pi} \left(2\mathcal{C}_{2L}^t - 2\mathcal{C}_{2R}^t \right) \\
&\quad + \frac{\alpha_w}{16\pi} \left((4 + \xi_t) \mathcal{C}_{2L}^t - \xi_t \mathcal{C}_{2R}^t - 4|V_{tb}|^2 \mathcal{C}_{3L}^b - 4V_{ts}^* V_{tb} \mathcal{C}_{4L} \right), \\
\mu \frac{d\mathcal{C}_{2R}^j}{d\mu} &= \frac{3\alpha_s C_F}{\pi} \mathcal{C}_1, \text{ for } j = (u, c), \\
\mu \frac{d\mathcal{C}_{2R}^t}{d\mu} &= \frac{3\alpha_s C_F}{\pi} \mathcal{C}_1 + \frac{\alpha_t}{16\pi} \left(-2\mathcal{C}_{2L}^t + 2\mathcal{C}_{2R}^t \right) \\
&\quad + \frac{\alpha_w}{16\pi} \left(-\xi_t \mathcal{C}_{2L}^t + (\xi_t + 2\xi_t |V_{tb}|^2) \mathcal{C}_{2R}^t - 2 \sum_{i=d,s,b} |V_{ti}|^2 \xi_t \mathcal{C}_{3L}^i - 2V_{ts}^* V_{tb} \xi_t \mathcal{C}_{4L} \right), \\
\mu \frac{d\mathcal{C}_{3L}^j}{d\mu} &= -\frac{3\alpha_s C_F}{\pi} \mathcal{C}_1 + \frac{\alpha_w}{16\pi} \left(-4 \sum_{i=u,c,t} |V_{ij}|^2 \mathcal{C}_{2L}^i - 2|V_{tj}|^2 \xi_t \mathcal{C}_{2R}^t + 4\mathcal{C}_{3L}^j \right. \\
&\quad \left. + 2 \sum_{i=d,s,b} V_{tj}^* V_{ti} \xi_t \mathcal{C}_{3L}^i + (1 - \delta_{dj}) (V_{ts}^* V_{tb} \xi_t) \mathcal{C}_{4L} \right), \text{ for } j = (d, s, b), \\
\mu \frac{d\mathcal{C}_{3R}^j}{d\mu} &= \frac{3\alpha_s C_F}{\pi} \mathcal{C}_1, \text{ for } j = (d, s, b), \\
\mu \frac{d\mathcal{C}_{4L}}{d\mu} &= \frac{3\alpha_s \alpha_w}{8\pi^2} (C_F V_{ts}^* V_{tb} \xi_t) \mathcal{C}_1 + \frac{\alpha_w}{16\pi} \left(-4 \sum_{i=u,c,t} (V_{is}^* V_{ib}) \mathcal{C}_{2L}^i - 2(V_{ts}^* V_{tb} \xi_t) \mathcal{C}_{2R}^t \right. \\
&\quad \left. + \sum_{i=d,s,b} (1 - \delta_{id}) (V_{ts}^* V_{tb} \xi_t) \mathcal{C}_{3L}^i + (4 + |V_{tb}|^2 \xi_t) \mathcal{C}_{4L} \right). \tag{3.36}
\end{aligned}$$

4 Finite terms

The matching coefficient for the $b \rightarrow sa$ operator written down at the M_W scale has mainly three components from the theory written down at the Λ scale. For clarity, we refer to this

²As pointed out in Ref. [69], redundant operators involving the axion and Higgs fields can universally contribute to the axion-fermion couplings leading to an effective $a\mu^+\mu^-$ interaction. We do not consider such leptonic interactions of axions because we find its branching fraction to be rather small compared to hadronic modes.

theory as the UV theory, acknowledging a minor terminological concession. The first term, denoted by f_1^{sw} , arises from the two-loop diagrams shown in Fig. 8. Similarly, the axion-diagonal quark operators also contribute to the same, generated by the one-loop process depicted in the leftmost diagram of Fig. 6. The final contribution, of course, comes from the overall counterterm, described by the operator $b - s - a$, shown in Fig. 11.

To compute the matching coefficient for the $b \rightarrow sa$ operator, we first have to evaluate the amplitude for the $b \rightarrow sa$ process in the UV theory, and we find

$$\begin{aligned} \mathcal{M}_{\text{UV}}(b \rightarrow sa) &= \sum_{j=1}^4 \mathcal{C}_j(\mu) \langle sa | \mathcal{O}_j(\mu) | b \rangle, \\ &= \mathcal{C}_{4L}(\mu) + \frac{\alpha_w}{16\pi} \sum_u \left\{ \mathcal{C}_{2L}^u(\mu) f_{2L}^{u,w}(\mu) + (L \rightarrow R) \right\} + \frac{\alpha_s}{4\pi} \frac{\alpha_w}{16\pi} \mathcal{C}_1(\mu) f_1^{sw}(\mu), \end{aligned} \quad (4.1)$$

where,

$$f_{2L}^{u,w}(\mu) = V_{su}^* V_{ub} \left[2 \log \left(\frac{\mu^2}{M_W^2} \right) + (2\xi_u - 1) - \frac{4\xi_u}{\xi_u - 1} \log \xi_u \right], \quad (4.2)$$

$$f_{2R}^{u,w}(\mu) = V_{su}^* V_{ub} \left[\xi_u \log \left(\frac{\mu^2}{M_W^2} \right) - \frac{\xi_u (\xi_u^2 - 2\xi_u + 4)}{(\xi_u - 1)^2} \log \xi_u - \frac{\xi_u (\xi_u - 7)}{2(\xi_u - 1)} \right], \quad (4.3)$$

and the two-loop matching coefficient is obtained as

$$\begin{aligned} f_1^{sw}(\mu) &= 6C_F \sum_u V_{su}^* V_{ub} \left[\left\{ \frac{2\xi_u (\xi_u^2 - 2\xi_u + 4) \log \xi_u}{(\xi_u - 1)^2} - \frac{2\xi_u (4\xi_u + 5)}{3(\xi_u - 1)} \right\} \log \left(\frac{\mu^2}{M_W^2} \right) \right. \\ &\quad - \xi_u \log^2 \left(\frac{\mu^2}{M_W^2} \right) - \frac{(4\pi^2 (\xi_u - 2) - 33\xi_u - 3) \xi_u}{6(\xi_u - 1)} - \frac{4\xi_u (-2\xi_u + 3(\xi_u - 2) \log(\xi_u - 1) - 3) \log \xi_u}{3(\xi_u - 1)} \\ &\quad + \frac{\xi_u (3\xi_u^2 - 10\xi_u + 1) \log^2(\xi_u)}{(\xi_u - 1)^2} + \frac{2(1 - 4\xi_u) \xi_u \text{Li}_2 \left(1 - \frac{1}{\xi_u} \right)}{(\xi_u - 1)^2} + \frac{4(\xi_u - 2) \xi_u \text{Li}_2 \left(\frac{1}{\xi_u} \right)}{\xi_u - 1} \\ &\quad \left. + \underbrace{\left\{ \xi_u \log \left(\frac{\mu^2}{M_W^2} \right) + \frac{3(\xi_u + 1) \xi_u}{2(\xi_u - 1)} - \frac{(\xi_u + 2) \xi_u^2 \log \xi_u}{(\xi_u - 1)^2} \right\} \log \left(\frac{\mu^2}{m_R^2} \right)}_{\text{IR-divergent}} \right], \end{aligned} \quad (4.4)$$

where the dilogarithm function is defined as $\text{Li}_2(x)$ in f_1^{sw}

$$\text{Li}_2(x) = - \int_0^x dt \frac{\log(1-t)}{t}. \quad (4.5)$$

We observe that there exist \log^2 terms in f_1^{sw} , which is an artifact of two loops. More importantly, although we were able to remove the pure UV poles and the mixed UV-IR poles, the finite piece f_1^{sw} still has pure IR divergences, shown with the underbrace. As expected, these IR divergences are of the form $\log m_R^2$ and therefore nonanalytic functions of the IR scale. However, both the UV and the EFT theories are local in the IR mass scale. Hence, a consistent matching condition is defined as:

$$\text{Matching condition: } \mathcal{M}_{\text{UV}} - \mathcal{M}_{\text{EFT}}, \quad (4.6)$$

should get rid of any IR divergences, and this is what we show in the next section.

5 Matching at the Electroweak Scale

In this section, we verify whether the IR divergent pieces shown in Eq. (4.4) indeed cancel out once we match the theory to the effective theory written at the M_W scale. Furthermore, the matching contribution to the Lagrangian, that is, $\mathcal{M}_{\text{UV}} - \mathcal{M}_{\text{EFT}}$, leads to a change in the EFT parameters. After integrating out the degrees of freedom (dof) heavier than the M_W scale, the effective Lagrangian is expressed as

$$\mathcal{L}_{\text{EFT}} = \mathcal{L}'_{\text{SM}} + \frac{1}{2} (\partial_\mu a)^2 - \frac{m_a^2}{2} a^2 + \sum_j \mathcal{C}'_j \mathcal{O}'_j, \quad (5.1)$$

where \mathcal{L}'_{SM} denotes the low energy SM Lagrangian. The operators are explicitly defined as:

$$\mathcal{O}'_1 = \mathcal{O}_1, \quad \mathcal{O}'_{2L/R} = \mathcal{O}_{2L/R}^u, \quad \mathcal{O}'_{3L/R} = \mathcal{O}_{3L/R}^d, \quad \mathcal{O}'_{4L} = \mathcal{O}_{4L}, \quad \mathcal{O}'_{5L} = \bar{s} i \not{D} P_L b, \quad (5.2)$$

with the covariant derivative $D_\mu = \partial_\mu - ig_s G_\mu^a T^a$ and $d = \{d, s, b\}$, but $u = \{u, c\}$ since here there is no top quark as a dof. The problem now is to compute the Wilson coefficients of the electroweak scale EFT, that is, \mathcal{C}'_i 's.

5.1 Generic Wilson coefficients of the EFT

We define the amplitudes for the initial to final state ($i \rightarrow f$) transition in the UV and the effective theory as

$$\mathcal{M}_{\text{UV}}(\mu) = \sum_{j=1}^4 \mathcal{C}_j(\mu) \langle \mathcal{O}_j(\mu) \rangle, \quad \mathcal{M}_{\text{EFT}}(\mu) = \sum_{j=1}^5 \mathcal{C}'_j(\mu) \langle \mathcal{O}'_j(\mu) \rangle. \quad (5.3)$$

where the shorthand notation describes $\langle \mathcal{O}_j(\mu) \rangle = \langle f | \mathcal{O}_j(\mu) | i \rangle$. The Wilson coefficients of the EFT, that is, \mathcal{C}'_i 's, can be determined by matching at the $\mu_w = m_W$ scale, that is, $\mathcal{M}_{\text{UV}}(\mu_w) = \mathcal{M}_{\text{EFT}}(\mu_w)$. We can now expand Eq. (5.3) order by order in α , leading to

$$\begin{aligned} \mathcal{C}'_j(\mu) &= \mathcal{C}'_j{}^{\text{tree}}(\mu) + \frac{\alpha_s}{4\pi} \mathcal{C}'_j{}^s(\mu) + \frac{\alpha_w}{16\pi} \mathcal{C}'_j{}^w(\mu) + \frac{\alpha_s}{4\pi} \frac{\alpha_w}{16\pi} \mathcal{C}'_j{}^{sw}(\mu), \\ \langle \mathcal{O}'_j(\mu) \rangle &= \langle \mathcal{O}'_j(\mu) \rangle^{\text{tree}} + \frac{\alpha_s}{4\pi} \langle \mathcal{O}'_j(\mu) \rangle^s + \frac{\alpha_w}{16\pi} \langle \mathcal{O}'_j(\mu) \rangle^w + \frac{\alpha_s}{4\pi} \frac{\alpha_w}{16\pi} \langle \mathcal{O}'_j(\mu) \rangle^{sw}, \\ \mathcal{M}_{\text{UV}}(\mu) &= \mathcal{M}_{\text{UV}}^{\text{tree}}(\mu) + \frac{\alpha_s}{4\pi} \mathcal{M}_{\text{UV}}^s(\mu) + \frac{\alpha_w}{16\pi} \mathcal{M}_{\text{UV}}^w(\mu) + \frac{\alpha_s}{4\pi} \frac{\alpha_w}{16\pi} \mathcal{M}_{\text{UV}}^{sw}(\mu). \end{aligned} \quad (5.4)$$

The superscript ‘*tree*’ implies the tree-level contribution of the corresponding operators. We reiterate that the terms proportional to α_s^2 contribute only as corrections to the RGE equations. In contrast, at the $\mathcal{O}(\alpha_s \alpha_w)$ order, new operators are generated, which is relevant for our phenomenological study. By applying the previously mentioned matching condition, we find the tree level as well as $\mathcal{O}(\alpha_s, \alpha_w)$ order components of the amplitude as

$$\mathcal{M}_{\text{UV}}^{\text{tree}}(\mu_w) = \mathcal{C}'_j{}^{\text{tree}}(\mu_w) \langle \mathcal{O}'_j(\mu_w) \rangle^{\text{tree}}, \quad (5.5)$$

$$\mathcal{M}_{\text{UV}}^{(s,w)}(\mu_w) = \mathcal{C}'_j{}^{\text{tree}}(\mu_w) \langle \mathcal{O}'_j(\mu_w) \rangle^{s,w} + \mathcal{C}'_j{}^{(s,w)}(\mu_w) \langle \mathcal{O}'_j(\mu_w) \rangle^{\text{tree}}. \quad (5.6)$$

In a similar way, $\mathcal{M}_{\text{UV}}^{(sw)}(\mu_w)$ has four contributions at the order $\mathcal{O}(\alpha_s \alpha_w)$. Plugging the relevant initial and final states into the matrix elements one can compute the \mathcal{C}'_i 's by solving these equations.

5.2 Evaluation of \mathcal{C}'_{4L}

For $b \rightarrow sa$ production, we only require the coefficient $\mathcal{C}'_{4L}(\mu_w)$. To determine this, the following components are required: $\mathcal{M}_{\text{UV}}(b \rightarrow sa)$, $\mathcal{M}_{\text{UV}}(b \rightarrow s)$, $\langle sa|\mathcal{O}'_j|b\rangle$, and $\langle s|\mathcal{O}'_j|b\rangle$ matrix elements. Collecting terms in order by order again, we find

1. Tree level Contribution:

The tree-level matching condition can be evaluated straightforwardly. For example, in the UV theory, the tree-level matrix element is given by

$$\mathcal{M}_{\text{UV}}^{\text{tree}}(b \rightarrow sa) = \mathcal{C}_{4L}(\mu_w) \langle sa|\mathcal{O}_{4L}(\mu_w)|b\rangle^{\text{tree}} , \quad (5.7)$$

Notice that both the UV theory and EFT have the same operator \mathcal{O}_{4L} . Therefore, upon using the matching condition given in Eq. (5.5), we find

$$\mathcal{C}'_{4L}{}^{\text{tree}}(\mu_w) = \mathcal{C}_{4L}(\mu_w) . \quad (5.8)$$

2. Contribution at $\mathcal{O}(\alpha_s)$ and $\mathcal{O}(\alpha_w)$:

At one-loop level, i.e., at the $\mathcal{O}(\alpha_s)$ and $\mathcal{O}(\alpha_w)$ order, the matrix elements for $b \rightarrow sa$ in the UV theory are

$$\begin{aligned} \frac{\alpha_w}{16\pi} \mathcal{M}_{\text{UV}}^w(b \rightarrow sa) &= \sum_u \mathcal{C}_{2L}^u(\mu_w) \langle sa|\mathcal{O}_{2L}^u(\mu_w)|b\rangle^w + (L \rightarrow R) , \\ &= \frac{\alpha_w}{16\pi} \sum_u [\mathcal{C}_{2L}^u(\mu_w) f_{2L}^{u,w}(\mu_w) + (L \rightarrow R)] \langle sa|\mathcal{O}_{4L}(\mu_w)|b\rangle^{\text{tree}} . \end{aligned} \quad (5.9)$$

Here the sum is over all the three up-type quark flavors. The finite pieces $f_{2L}^{u,w}$ and $f_{2R}^{u,w}$ have already been computed by the insertion of \mathcal{O}_{2L} and \mathcal{O}_{2R} operators in the first diagram of Fig. 6 and by adding the $b \rightarrow sa$ counter term.

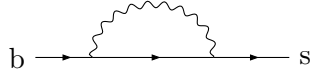


Figure 12. Diagram for the finite term f_{bs}^w .

Similarly, at $\mathcal{O}(\alpha_w)$ order, we generate the $b \rightarrow s$ transition as shown in Fig. 12, and the corresponding amplitude is

$$\frac{\alpha_w}{16\pi} \mathcal{M}_{\text{UV}}^w(b \rightarrow s) = \frac{\alpha_w}{16\pi} f_{bs}^w(\mu_w) \langle s|\mathcal{O}'_{5L}(\mu_w)|b\rangle^{\text{tree}} . \quad (5.10)$$

Although this does not generate axions directly, insertions of such diagrams would indeed generate $b \rightarrow sa$. We remind the reader that we have already used insertions of such operators ($1/\epsilon$ pieces) to cancel the UV divergence. Therefore, to match and cancel the purely IR divergent contributions, we only require the finite term from Fig. 12, given by

$$f_{bs}^w(\mu) = \sum_u V_{su}^* V_{ub} \left[\xi_u \log \left(\frac{\mu^2}{M_W^2} \right) + \frac{3\xi_u(\xi_u + 1)}{2(\xi_u - 1)} - \frac{\xi_u^2(\xi_u + 2) \log \xi_u}{(\xi_u - 1)^2} \right] . \quad (5.11)$$

In the EFT, W -boson ceases to be a dynamic degree of freedom which implies the matrix element $\langle sa|\mathcal{O}'_j|b\rangle^w = 0$ and no flavor changing neutral current (FCNC) is possible at the tree level, rendering the Wilson coefficient $\mathcal{C}'_{4L}{}^{\text{tree}} = 0$. Therefore the one-loop matching condition from Eq. (5.6) gives

$$\mathcal{C}'_{4L}{}^w(\mu_w) = \mathcal{C}_{2L}(\mu_w)f_{2L}^w(\mu_w) + (L \rightarrow R) , \quad \text{and} \quad \mathcal{C}'_{5L}{}^w(\mu_w) = f_{bs}^w(\mu_w) . \quad (5.12)$$

We note in passing that $\mathcal{O}(\alpha_s)$ and $\mathcal{O}(\alpha_{\text{em}})$ corrections are same in the UV and IR theory and therefore would cancel after matching.

3. Contribution at $\mathcal{O}(\alpha_s\alpha_w)$ order:

Finally, for the two-loop matrix element in UV, the theory for $b \rightarrow sa$, the only contribution comes from the \mathcal{O}_1 operator, which is

$$\begin{aligned} \frac{\alpha_s}{4\pi} \frac{\alpha_w}{16\pi} \mathcal{M}_{\text{UV}}^{sw}(b \rightarrow sa) &= \mathcal{C}_1(\mu_w) \langle sa|\mathcal{O}_1(\mu_w)|b\rangle^{sw} , \\ &= \frac{\alpha_s}{4\pi} \frac{\alpha_w}{16\pi} \mathcal{C}_1(\mu_w) f_1^{sw}(\mu_w) \langle sa|\mathcal{O}_{4L}(\mu_w)|b\rangle^{\text{tree}} , \end{aligned} \quad (5.13)$$

where the finite term $f_1^{(sw)}$ is evaluated by adding all the two-loop diagrams, its corresponding one-loop counter terms, and the overall counter terms, as illustrated in section 3.2.4. On the other hand, the matching condition with all the non-zero contributions from the EFT gives

$$\begin{aligned} \mathcal{M}_{\text{UV}}^{sw}(b \rightarrow sa) &= \mathcal{C}'_{5L}{}^w(\mu_w) \langle sa|\mathcal{O}'_{5L}(\mu_w)|b\rangle^s + \mathcal{C}'_{4L}{}^{sw} \langle sa|\mathcal{O}_{4L}(\mu_w)|b\rangle^{\text{tree}} , \\ &= (\mathcal{C}'_{5L}{}^w(\mu_w) f_{4L}^s(\mu_w) + \mathcal{C}'_{4L}{}^{sw}) \langle sa|\mathcal{O}_{4L}(\mu_w)|b\rangle^{\text{tree}} . \end{aligned} \quad (5.14)$$

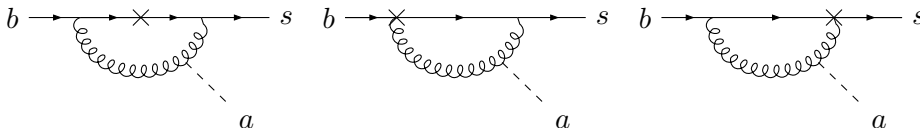


Figure 13. Diagrams for f_{4L}^s . The cross denotes the \mathcal{O}'_{4L} operator insertion.

where Fig. 13 gives the following amplitude

$$f_{5L}^s(\mu) = 6C_F \mathcal{C}_1(\mu) \left[\log\left(\frac{\mu^2}{m_R^2}\right) + \frac{1}{3} \right] . \quad (5.15)$$

Finally, comparing Eqs. (5.13) and (5.14), we obtain

$$\mathcal{C}'_{4L}{}^{sw}(\mu_w) = \mathcal{C}_1(\mu_w) f_1^{sw}(\mu_w) - f_{bs}^w(\mu_w) f_{5L}^s(\mu_w) . \quad (5.16)$$

We already saw that in the two-loop finite term $f_1^{(sw)}(\mu)$ has IR divergence pieces $\log(\mu^2/m_R^2)$. However, the EFT at the scale M_W has the same IR structure as in the second term of the equation ((5.16)). Therefore, the final Wilson coefficient contribution from the two-loop

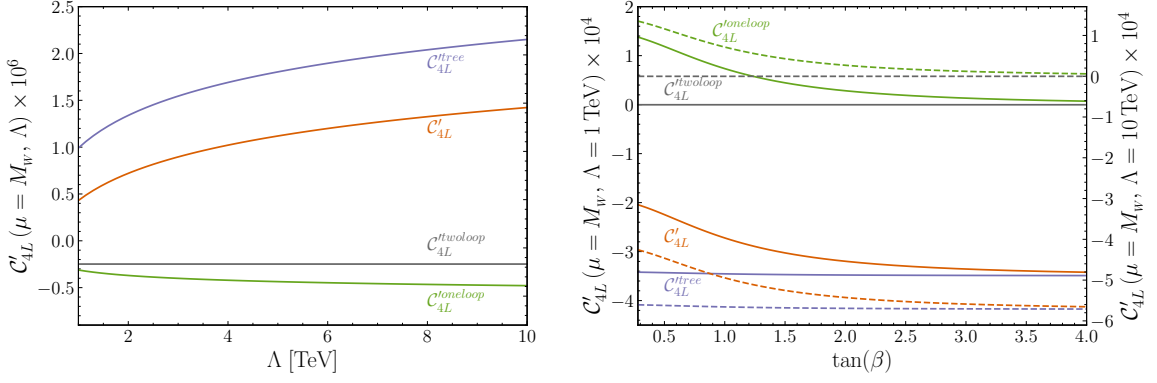


Figure 14. Left: The $C'_{4L}(M_W)$ for the various values of UV scale (Λ) in the KSVZ model. Right: The $C'_{4L}(M_W)$ for different values of $\tan(\beta)$ in the DFSZ model with the solid line for $\Lambda = 1$ TeV (left axis) and dashed line for $\Lambda = 10$ TeV (right axis). Violet, green, grey, and orange lines correspond to the tree, one loop, two loop, and total contribution to the $C'_{4L}(M_W)$, Eq. (5.17), respectively.

diagrams has no IR divergence because it cancels through the matching. Therefore, the total contribution to the $C'_{4L}(\mu_w)$ is

$$\boxed{C'_{4L}(\mu_w) = C_{4L}(\mu_w) + \frac{\alpha_w}{16\pi} C_{4L}^{lw}(\mu_w) + \frac{\alpha_s}{4\pi} \frac{\alpha_w}{16\pi} C_{4L}^{lsw}(\mu_w).} \quad (5.17)$$

Plugging all the finite terms in Eq. (5.12) and Eq. (5.16) respectively, we get

$$\begin{aligned} C_{4L}^{lw}(\mu_w) &= \sum_u V_{su}^* V_{ub} \left[C_{2L}^u(\mu_w) \left\{ (2\xi_u - 1) - \frac{4\xi_u}{\xi_u - 1} \log \xi_u \right\} \right. \\ &\quad \left. - C_{2R}^u(\mu_w) \left\{ \frac{\xi_u (\xi_u^2 - 2\xi_u + 4)}{(\xi_u - 1)^2} \log \xi_u + \frac{\xi_u (\xi_u - 7)}{2(\xi_u - 1)} \right\} \right], \\ C_{4L}^{lsw}(\mu_w) &= 6C_F \sum_u V_{su}^* V_{ub} C_1(\mu_w) \left[\frac{\xi_u \{15\xi_u - 2\pi^2(\xi_u - 2)\}}{3(\xi_u - 1)} + \frac{\xi_u (3\xi_u^2 - 10\xi_u + 1)}{(\xi_u - 1)^2} \log^2 \xi_u \right. \\ &\quad \left. - \frac{\xi_u \{-3\xi_u^2 + 4(\xi_u^2 - 3\xi_u + 2) \log(\xi_u - 1) - 2\xi_u + 4\}}{(\xi_u - 1)^2} \log \xi_u \right. \\ &\quad \left. + \frac{4\xi_u(\xi_u - 2)}{\xi_u - 1} \text{Li}_2\left(\frac{1}{\xi_u}\right) + \frac{2\xi_u(1 - 4\xi_u)}{(\xi_u - 1)^2} \text{Li}_2\left(1 - \frac{1}{\xi_u}\right) \right]. \end{aligned} \quad (5.18)$$

Below M_W , running effects due to W , Z bosons and top quark are absent as these heavy particles are integrated out. Consequently, C'_{4L} , the $b \rightarrow sa$ Wilson coefficient does not run below M_W , so $C'_{4L}(\mu_\chi) = C'_{4L}(\mu_w)$ where $\mu_\chi \sim 1 - 2$ GeV. All other Wilson coefficients run at $\mathcal{O}(\alpha_s)$, barring the electroweak contributions, as given in Eq. (3.36).

In Fig. 14, we show the relative contributions of the Wilson coefficient in Eq. (5.17). On the left-hand side, we present the values of $C'_{4L}(M_W)$ in the KSVZ-like model for various values of the UV scale. The reason for the inverted feature of the Wilson coefficients compared to [71] is attributed to the absorbance of a sign in the previous work. On the

other hand, the figure on the right depicts the values of $\mathcal{C}'_{4L}(M_W)$ as a function of $\tan\beta$. We show only the results until $\tan\beta = 4$, as the Wilson coefficient is almost insensitive to larger values of $\tan\beta$. The solid lines, blue (tree level), orange (one loop), green (two loop), and red (full contribution), are for $\Lambda = 1$ TeV with their corresponding values presented in the left axis. The same is presented for $\Lambda = 10$ TeV with the corresponding values presented on the right axis. This concludes our discussion of the theoretical framework. Before presenting our results, we will first review the existing experimental searches relevant to our framework.

6 Axion Decays and Branching Fractions

Before discussing the limits on the axion parameter space, it is necessary to first discuss the meson-level decay width for the $B \rightarrow Ka$ process. We find it to be

$$\Gamma_{B \rightarrow Ka} = |\mathcal{C}'_{4L}(M_W)|^2 \frac{m_B^3}{64\pi f_a^2} \left(1 - \frac{m_K^2}{m_B^2}\right)^2 \lambda_{Ka}(m_a) f_0(m_a)^2, \quad (6.1)$$

where λ_{Ka} is the usual Källén function, defined as

$$\lambda_{Ka}(m_a) = \left[\left(1 - \frac{(m_K + m_a)^2}{m_B^2}\right) \left(1 - \frac{(m_K - m_a)^2}{m_B^2}\right) \right]^{1/2}, \quad (6.2)$$

and the form factor from lightcone QCD sum rules is given by

$$f_0(m_a) = \frac{0.330}{1 - [m_a(\text{GeV})]^2/37.5}. \quad (6.3)$$

We note in passing that there exists an uncertainty of 10% in the light-cone form factor.

The produced axion would also decay to various hadronic modes. Therefore, in this section, we provide axion decay widths and branching fractions for the KSVZ, DFSZ, and Flaxion models. We use these results in the next section to draw constraints on the space of axion parameters, i.e., the $m_a - f_a$ plane. We take only the most dominant channels such as $a \rightarrow \pi\pi\eta$, $KK\pi$, 3π , $\phi\phi$, and $\gamma\gamma$. However, other hadronic modes are also presented in Fig. 15 for completeness. To derive the branching fractions, we follow the analysis of [101] and modify it according to our framework. Detailed calculations are provided in the appendix E where ChPT and vector meson dominance are used for matching with the QCD-axion Lagrangian (E.1) at the $\mu_\chi \approx 1 - 2$ GeV scale. Note that the parameters of the QCD-axion Lagrangian are RG evolved with appropriate boundary conditions for different axion-UV models. For the decay widths, we choose the UV scale at 1 TeV. Since the branching fractions do not vary much with different choices of the UV scales, we use this to give the bounds on the axion parameter space. This framework is then subsequently used to determine the relevant axion decay amplitudes.

As can be seen in Fig. 15, the decay width and branching fractions for the $a \rightarrow \gamma\gamma$ channel differ around $m_a = 2.1$ GeV for different UV frameworks. This is an artifact of switching off the vector meson-dominance (VMD), whereas the perturbative QCD contribution becomes relevant for $m_a > 2.1$ GeV. However, in this region, the differences among

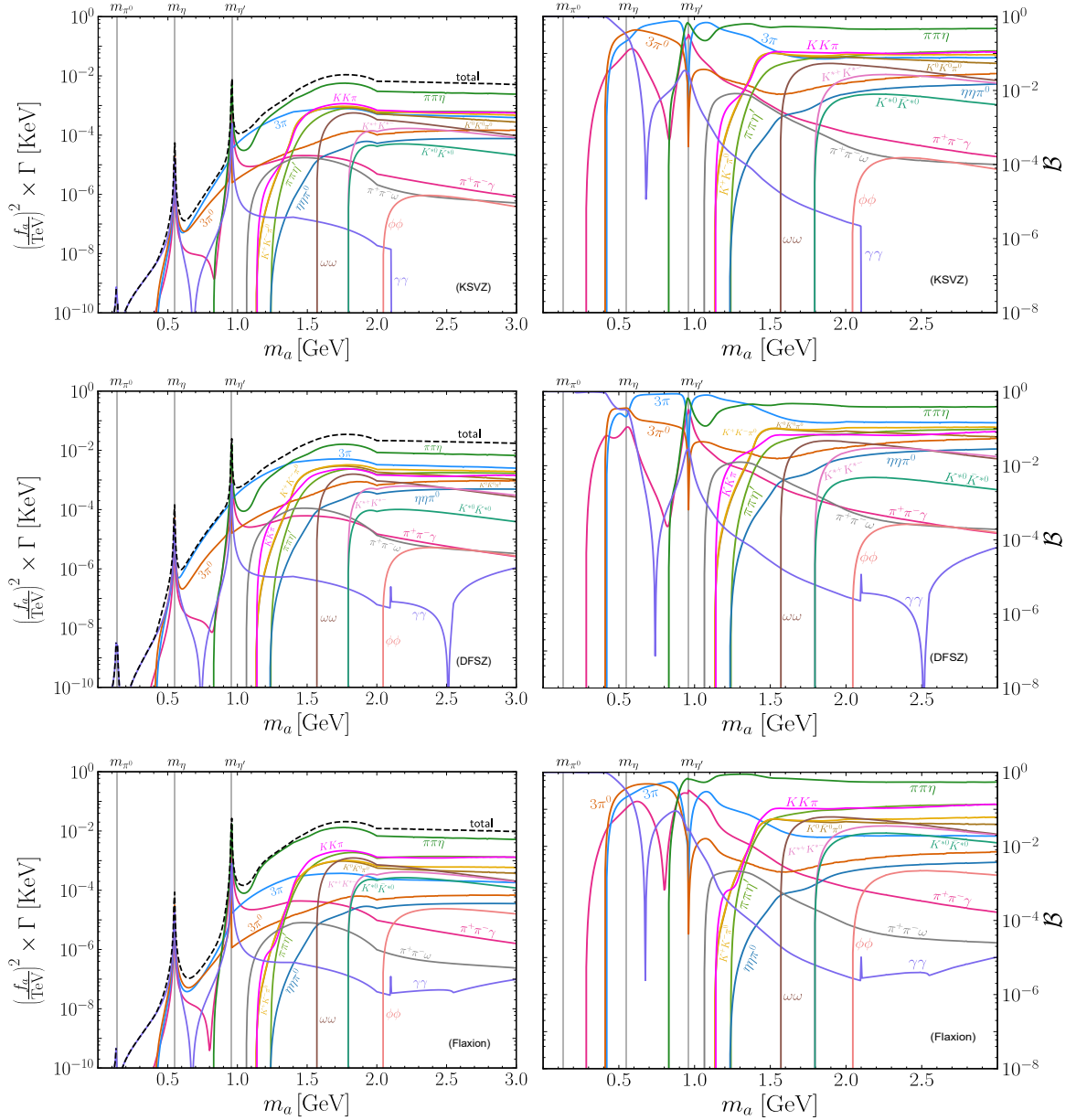


Figure 15. Axion decay widths (left) and branching fractions (right) in KSVZ, DFSZ, and Flaxion models. The total decay width is the sum of these modes, represented by the black dashed curve. 3π denotes the channel $(\pi^+\pi^-\pi^0)$. Furthermore, the $\pi\pi\eta$, $\pi\pi\eta'$ and $KK\pi$ labels denote the combined channels $(\pi^0\pi^0\eta + \pi^+\pi^-\eta)$, $(\pi^0\pi^0\eta' + \pi^+\pi^-\eta')$, and $(K^+\bar{K}^0\pi^- + K^-K^0\pi^+)$ respectively.

the different UV scenarios are mainly attributed to the RG evolved values $\mathcal{C}_{qq}(\mu_\chi)$. For the other modes, the only contribution comes from ChPT and VMD. This changes only the decay widths and branching fractions quantitatively, but not qualitatively. The peaks around m_{π^0} , m_η , and $m_{\eta'}$ appear due to the divergent nature of the mixing with the axion field; see Eq. (E.10).

7 Experimental Searches and Projections

Our analysis focuses exclusively on the hadronic interactions of axions, suggesting that the majority of decay channels for the ALP will be hadronic. Additionally, because of interactions between axions and pions, the axion may also decay into two photons. The branching fractions for these decay modes were evaluated in a data-driven approach in Ref. [45].

Axion searches can generally be categorized into two types: prompt and displaced. For larger coupling constants or smaller values of f_a , the axions decay at the primary vertex, resulting in prompt signals. In contrast, for larger values of f_a , the axion lifetime is extended, leading to displaced vertex signatures. The SM background for such processes is relatively small, providing an additional opportunity to probe the axion or ALP parameter space. If the axion has a decay length longer than the dimensions of the detector, it would produce missing-energy signals. However, this scenario implies an even smaller coupling for the axion compared to the displaced topology, resulting in a reduced production cross-section. We first discuss the inclusive $b \rightarrow sa$ process followed by tabulating different prompt decays from axions.

7.1 Inclusive $b \rightarrow sa$ process

We first draw constraints from the $b \rightarrow sa$ inclusive process. According to the Particle Data Group, any non-standard decay mode of the B -meson should exhibit a branching fraction $< 11\%$ [102]. This inclusive process is devoid of any hadronic uncertainties and, therefore, extremely robust. The relevant constraints are illustrated by a yellow region in the accompanying plots. For exclusive processes, we also considered the branching fractions of the axions into various final states [45].

7.2 Present Constraints

For the present bounds, we mainly consider axions with shorter lifetimes that give rise to prompt decay modes. We note down all the relevant possibilities below.

1. $B \rightarrow Ka (a \rightarrow \gamma\gamma)$: For this particular final state, we follow the strategy from [72] where results from BABAR [103] on the branching fraction $\text{Br}(B \rightarrow Ka) \times \text{Br}(a \rightarrow \gamma\gamma)$, in the region $0.175 \text{ GeV} < m_a < 4.78 \text{ GeV}$ were revised for heavy QCD axions. Note that, in Ref. [103], bounds are expressed for different axion lifetimes such as $c\tau_{\text{BBR}}(m_a, f_a) = 0, 0.1, 1$ and 10 cm . We took a conservative approach and excluded any values of m_a, f_a , and the corresponding $c\tau_a$ if it is already excluded by the BABAR analysis satisfying $c\tau_{\text{BBR}} \geq c\tau_a$. We show this exclusion in the *slateblue* shaded region of our plots, i.e., Figs. 16, 17 and 18.
2. $B \rightarrow Ka (a \rightarrow \pi\pi\eta)$: Ref. [104] reported the branching fractions of $B^+ \rightarrow \eta_X K^+$, where the η_X subsequently decays to $\pi\pi\eta(\pi^0\pi^0\eta + \pi^+\pi^-\eta)$. The identification of B -meson candidates was achieved through several kinematic cuts, for example, $1.2 \text{ GeV} < m_{\pi\pi\eta} < 1.5 \text{ GeV}$, etc. This invariant mass region is strategically chosen to include a broad spectrum of states below the charm production threshold. From the final reported result,

the following constraint [45] was derived $\text{Br}(B^\pm \rightarrow K^\pm a) \times \text{Br}(a \rightarrow \pi\pi\eta) < 2 \times 10^{-6}$. Instead of assuming this branching fraction, we follow the strategy of Ref. [71]. The experimental collaboration [104] reported events from $B^+ \rightarrow \eta\pi\pi K^+$ data in a bin size of 6.7 MeV. Motivated by this, we assumed the axion to be present at the boundary of adjacent bins. This is followed by the assumption that the number of events generated by the decay of the axions should be less than the sum of central values in addition to a 2σ uncertainty of these two bins. As a result, we correct for any spilling-over effects due to smearing. As shown in Figs. 16, 17 and 18, this region provides the strongest bound shown in *green* to rule out significant parts of the parameter space in our plots.

3. $B \rightarrow Ka(a \rightarrow KK\pi)$: Similar to the previous channel, Ref. [104] also studied the following decay channel $\eta_X \rightarrow KK\pi$ with the cut on the invariant mass of the $K\pi$ pair $0.85 \text{ GeV} < m_{K\pi} < 0.95 \text{ GeV}$. This result roughly translates to $\text{Br}(B^\pm \rightarrow K^\pm a) \times \text{Br}(a \rightarrow K^\pm K_S \pi^\mp) < 1 \times 10^{-7}$ [45]. This particular final state has also been looked at by LHCb using 3fb^{-1} data [105]. However, their sensitivity remains well below the BaBar experiment. For our purpose, we use the same methodology as discussed for the search $a \rightarrow \pi\pi\eta$. Constraints drawn from this search are shown in *pink* in our plots.
4. $B \rightarrow Ka(a \rightarrow \phi\phi)$: BaBar experiment studied the branching fraction and CP asymmetry for $B \rightarrow K\phi\phi$ decay [106] and found to be around 4.5×10^{-6} . Ref. [45] assumed the entire decay process is due to axions and estimated $\text{Br}(B \rightarrow Ka) \times \text{Br}(a \rightarrow \phi\phi) < 6 \times 10^{-6}$. For this particular channel, we assumed the axion to be present in the center of each bin as [106] provides their results in a bin of width 125 MeV. Because of this large bin width, the spilling-over effect due to Gaussian smearing is expected to be well within each of these bins. Finally, we assume that the signal generated from the axion decay is less than the central value augmented with a 2σ uncertainty. Using this formalism, we exclude the *orange* region in our plots.
5. $B \rightarrow Ka(a \rightarrow 3\pi)$: The constraint for this particular channel has been derived using the Belle analysis [107], applicable only in the tiny mass window $0.73 \text{ GeV} - 0.83 \text{ GeV}$. Recasting their analysis results in a branching fraction $\text{Br}[B \rightarrow Ka(a \rightarrow \pi^+\pi^-\pi^0)] < 4.9 \times 10^{-6}$, derived from $\text{Br}(\omega \rightarrow 3\pi) = 89\%$ and $\text{Br}(B^0 \rightarrow K^0\omega) < 5.5 \times 10^{-6}$. We use this result to exclude regions shown in *blue*.

A crucial point to note is that for searches where the axion decays to $\eta\pi\pi$, $KK\pi$, $\phi\phi$ and 3π , the bounds were roughly stronger by 10% by performing a bin-by-bin analysis rather than using a fixed branching fraction [71].

7.3 Future Projections

For future projections, we only use the following prompt signatures

7.3.1 $a \rightarrow \pi\pi\eta$ and $a \rightarrow 3\pi$:

For prompt signatures, we take the strongest limits coming from $a \rightarrow \pi\pi\eta$. As suggested in [71], we extrapolated the background provided in [104] and scaled it with the expected

luminosity of Belle II with 5×10^{10} $B\bar{B}$ pairs. After computing the standard deviation, we assume that the signal from the axion decay should be below the significance 2σ . Similarly, we also follow the same procedure for the $a \rightarrow \pi^+\pi^-\pi^0$ channel. In both cases, the experimental resolution of the axion mass is estimated to be $\delta m_a \sim 13.4$ MeV and 40 MeV, respectively, where $\delta m_a \sim \delta m_{\eta\pi\pi} m_a / m_{\eta'}$.

7.3.2 $a \rightarrow \gamma\gamma$:

For projection of the $a \rightarrow \gamma\gamma$ channel, we relax the condition of $c\tau_a < 10$ cm, as this constraint is too conservative given the size of the Belle II calorimeter. Thereafter, we follow the strategy from [72], where the photon is assumed to be produced promptly at the primary vertex for all lifetime values of the axion. However, the displaced photon analysis is incorporated by assuming a downward smearing on the axion mass, given by

$$m_{\gamma\gamma} \simeq m_a (1 - r/S) , \quad r = \frac{ct_a p_a}{m_a} , \quad (7.1)$$

where r is the flight distance of the axion, $p_a \sim 2.5$ GeV, is a typical axion momentum. $S \sim 120$ cm, which is roughly the distance between the interaction point and the face of the calorimeter. This translates to a $m_{\gamma\gamma}$ distribution of the form

$$\frac{dN}{dm_{\gamma\gamma}} = \frac{S}{p_a c \tau_a} \text{Exp} \left[\frac{S}{p_a c \tau_a} (m_{\gamma\gamma} - m_a) \right] \Theta (m_a - m_{\gamma\gamma}) , \quad (7.2)$$

We take into account the detector resolution by convoluting this distribution with a Gaussian of width $\sigma_{m_{\gamma\gamma}} \simeq 0.02 m_{\gamma\gamma}$ [108, 109]. The expected signal (N_S) and background (N_B) events are calculated following ref. [72] and finally, the projection in the $m_a - f_a$ plane is shown by pink dashed lines when $N_S / \sqrt{N_B} > 2$.

It is important to mention that the signatures of the displaced vertex are also important, as was shown in [72]. However, a dedicated study for different UV frameworks considering all channels is required, and we defer this to future work.

8 Results and Discussions

In this section, we present our results for different UV scenarios, such as KSVZ, DFSZ, and flavorful axions. The primary difference is the UV boundary condition for the relevant operators defined in Eq. (2.2).

8.1 KSVZ-Like Model

The KSVZ model [82, 83] is described in terms of the UV Lagrangian with a heavy non-SM fermion Q transforming in the fundamental representation of $SU(3)_c$, a singlet representation of $SU(2)_L$ and neutral under hypercharge $U(1)_Y$.

$$\mathcal{L}_{\text{KSVZ}} = |\partial_\mu \Phi|^2 + \bar{Q} i \not{D} Q - (y_Q \bar{Q}_L Q_R \Phi + h.c.) - V(\Phi) . \quad (8.1)$$

Eq. (8.3) has a global symmetry $U(1)_{PQ}$. After spontaneous symmetry breaking, the scalar field Φ acquires a vacuum expectation value $f_a / \sqrt{2}$, and the corresponding Goldstone

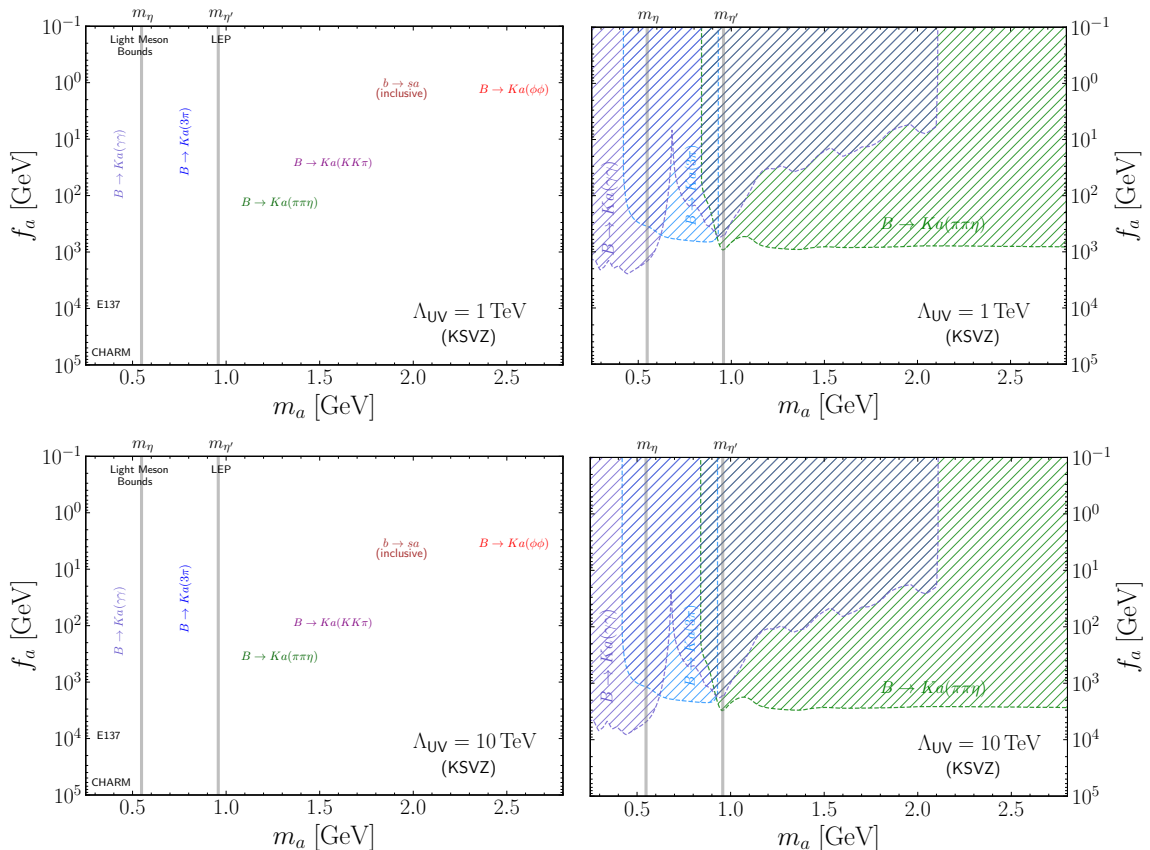


Figure 16. Left panel: We provide constraints on the axion parameter space by solid colored regions by considering the $\Lambda_{UV} = 1$ and 10 TeV respectively. Noticeable constraints come from axion production from B -meson and its subsequent prompt decays to $\gamma\gamma$ [103] (slate-blue), $\pi\pi\eta$ [104, 105] (green), $KK\pi$ [104] (pink), $\phi\phi$ [106] (orange) and 3π (blue) [106]. The grey shaded region collectively rules out parameter space from light meson decays [45, 47, 55, 61–63] and beam dump experiments [19–21] (also see [71, 72] for a similar study). Right panel: The future projections from Belle with 3 ab^{-1} data are shown in dashed lines using prompt decays of the ALP.

mode is identified as the axion. To obtain the interactions of the axion, one can perform the following chiral transformation on the heavy quark fields

$$Q \rightarrow e^{-i\gamma_5 a/2f_a} Q. \quad (8.2)$$

Under such a transformation, the measure of the action is not invariant and it picks up the QCD anomaly term

$$\mathcal{L}_{\text{KSVZ}} \supset \frac{\alpha_s}{8\pi f_a} a G \tilde{G}. \quad (8.3)$$

Eq. (8.3) gives us the matching coefficient for our operators defined in Eq. (2.2) at the Λ_{UV} scale. Therefore, we get

$$\mathcal{C}_1 = \frac{\alpha_s(\Lambda_{UV})}{8\pi}, \quad \mathcal{C}_{2L/R}^i = \mathcal{C}_{3L/R}^i = \mathcal{C}_{4L} = 0. \quad (8.4)$$

Note that $\mathcal{C}_{2L/R}^i$, along with the operators, can be generated via loops. In [10], such loop-induced UV values were considered for the quark operators, and the sensitivity to UV values was explicitly demonstrated in the exclusion plots. We have verified the same. However, we present our results assuming that only the $a - G - \tilde{G}$ operator is present in the UV. For such a scenario, the shaded regions in Fig. 16 show the present bounds on f_a coming from several hadronic final-state searches. The dashed lines represent the projected limits on f_a using the $3ab^{-1}$ data, which is also the projected luminosity of Belle II.

Notice that in the literature, sometimes bounds are provided by assuming $\Lambda = f_a$ or $4\pi f_a$. We have checked that, for the former scenario, we do not get any bounds at all. However, for the other cases as well as for projections, we can indeed exclude certain parts of the ALP parameter space, as illustrated in the Appendix C. The primary reason for obtaining a bound in this case is that we treat the UV scale and f_a independently. As a result, large logarithms from RG running contribute to the Wilson coefficients. However, because of the choice $\Lambda = f_a$, such large logs are absent. Furthermore, the choice $\Lambda = 4\pi f_a$ is motivated by a strongly coupled UV theory, which defeats the purpose of a weakly coupled UV framework to solve the strong-CP problem. Nevertheless, we remain agnostic about the UV framework and use only the UV values of the Wilson coefficient motivated by KSVZ. Finally, from Fig. 16, we conclude that roughly 100 GeV and 1 TeV values of f_a can already be excluded from the present intensity frontier data. This is similar to the limits obtained in [71].

8.2 DFSZ-Like Model

The DFSZ model [7, 84] uses a complex scalar field Φ to decouple the PQ symmetry-breaking scale from the electroweak scale. However, unlike KSVZ, it implements the QCD anomaly as in the Weinberg-Wilczek model through SM quarks charged under PQ symmetry. Thus, two Higgs doublets H_u and H_d are introduced, having Yukawa couplings with SM quarks and leptons.

After the PQ -symmetry breaks, the three scalar fields (Φ, H_u, H_d) get the corresponding vev and Goldstone modes. The physical axion field a and its vev v_a are defined as a combination of the three. During the calculation of PQ charges, the relation $v_u^2 + v_d^2 = v^2$ where $v \sim 246$ GeV is used and one defines $\sin\beta \equiv v_u/v, \cos\beta \equiv v_d/v$. Again, by an axion-field dependent redefinition, now of the lepton and quark fields, the mass terms get rid of axions, and one gets the QCD anomaly term $a - G - \tilde{G}$. In addition, under the redefinition, the axion gets derivatively coupled to the SM quarks and leptons through their kinetic terms. Hence, the following relevant couplings are generated in the DFSZ model:

$$\mathcal{L}_{\text{DFSZ}} \supset \frac{\alpha_s}{8\pi} \frac{a}{f_a} G\tilde{G} + C_u \frac{\partial_\mu a}{2f_a} \bar{u}\gamma^\mu\gamma_5 u + C_d \frac{\partial_\mu a}{2f_a} \bar{d}\gamma^\mu\gamma_5 d, \quad (8.5)$$

with $C_u = \cos^2\beta/3, C_d = \sin^2\beta/3$ and the axion decay constant is $f_a = v_a/6$ here. This means in DFSZ, our Wilson coefficients at Λ_{UV} are

$$\mathcal{C}_1 = \frac{\alpha_s(\Lambda_{\text{UV}})}{8\pi}, \mathcal{C}_{2L}^i = -\frac{\cos^2\beta}{6}, \mathcal{C}_{2R}^i = \frac{\cos^2\beta}{6}, \mathcal{C}_{3L}^i = -\frac{\sin^2\beta}{6}, \mathcal{C}_{3R}^i = \frac{\sin^2\beta}{6}, \mathcal{C}_{4L} = 0, \quad (8.6)$$

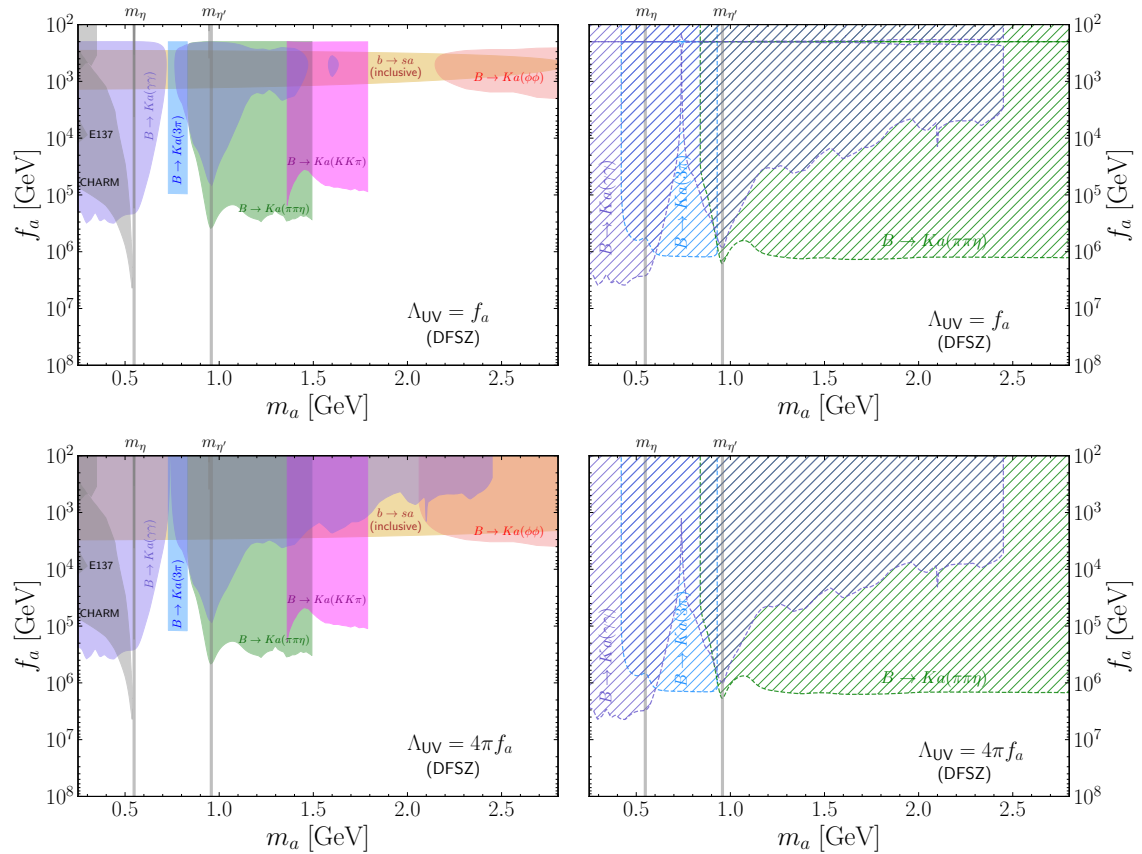


Figure 17. Left panel: Limits on the axion parameter space corresponding to the DFSZ model having initial conditions Eq. (8.6) with $\tan\beta = 0.28$. Right panel: The future projections from Belle, shown in dashed lines using both prompt decay signatures. The shaded regions and dashed lines are to be interpreted similarly to the bounds obtained in the KSVZ model Fig. 16.

where we have used $\gamma_5 = P_R - P_L$. The unitarity bound on the scattering amplitude of fermions translates to the following bound on β as [110]

$$\tan\beta \in [0.28, 140] . \quad (8.7)$$

For a typical value of $\tan\beta = 0.28$, we show the constraints on the $m_a - f_a$ plane for DFSZ-like scenarios in the left panel of Fig. 17. The projections are provided on the right panel with 3 ab^{-1} data. Unlike the KSVZ framework, here the flavor violation is generated at the one-loop level, which translates to much stronger limits on f_a . Notice an island-like region for the top left plot shown in Fig. 17. This is an artifact of the variation of $|\mathcal{C}'_{4L}(M_W)|^2$ as a function of f_a , where the Wilson coefficient itself varies from negative to positive values. This is due to the interplay between different signs in the loop-induced and tree-level Wilson coefficients. Moreover, the expression for the branching fraction explicitly depends on $1/f_a^2$. The cumulative features enable us to investigate higher values of f_a as depicted in the shaded island region.

8.3 Flavorful Axion Model

In this model [73], the axion emerges as the Goldstone mode of a scalar field of the BSM complex ϕ (called *flavon*). The model is constructed economically. The flavon field also addresses the flavor structure of the SM, via the Froggatt-Nielsen mechanism [78]. So, the global Abelian flavor symmetry: $U(1)_F$ that generates the Yukawa couplings also acts as the PQ symmetry. Under $U(1)_F$, we use their explicit charge assignment to left-handed quark doublets q_{Q_i} and right-handed singlets q_i :

$$\begin{pmatrix} q_{Q_1} & q_{Q_2} & q_{Q_3} \\ q_u & q_c & q_t \\ q_d & q_s & q_b \end{pmatrix} = \begin{pmatrix} 3 & 2 & 0 \\ -5 & -1 & 0 \\ -4 & -3 & -3 \end{pmatrix}. \quad (8.8)$$

After $U(1)_F$ and electroweak symmetry-breaking, the axion couples to quarks and leptons. A biunitary transformation diagonalizes the masses and Higgs-Yukawa interactions. However, the flavor-dependent $U(1)_F$ charges of the quarks/leptons lead to flavor-violating axion couplings even after transformation to the mass basis. These couplings are given by

$$\mathcal{L} \supset -\frac{ia}{\sqrt{2}v_\phi} \left(\kappa_{ij}^u \bar{u}_{Li} u_{Rj} + \kappa_{ij}^d \bar{d}_{Li} d_{Rj} \right). \quad (8.9)$$

After obtaining κ^u, κ^d from [73] and converting our UV axion couplings to this form (via integration by parts and Dirac equations for the quarks), we arrive at the following UV conditions ³

$$\begin{aligned} \mathcal{C}_1 &= \frac{\alpha_s(\Lambda_{UV})}{8\pi}, & \mathcal{C}_{2L}^u &= -0.165, & \mathcal{C}_{2L}^c &= -0.0577, & \mathcal{C}_{2L}^t &= -3.61 \times 10^{-6}, \\ \mathcal{C}_{3L}^d &= -0.293, & \mathcal{C}_{3L}^s &= -0.200, & \mathcal{C}_{3L}^b &= -0.0578, & \mathcal{C}_{4L} &= -0.00635, \\ \mathcal{C}_{2R}^i &= -\mathcal{C}_{2L}^i, & \mathcal{C}_{3R}^i &= -\mathcal{C}_{3L}^i. \end{aligned} \quad (8.10)$$

Here we have used the relation $\sqrt{2}v_\phi = f_a \times N_{DW}$ where the domain-wall number $N_{DW} = 26$ for this Flaxion model. As the couplings in this model depend on the ratios of quark masses, the approximation $m_i \sim 0$ for i other than the top quark is relaxed. We take the quark masses from Ref. [110]. Finally, we present our results in the left panel and projections in the right panel of Fig. 18. The input parameters used for Figs. 16, 17 and 18 are given in Appendix D.

For both DFSZ and Flaxion models, we present our bounds and projections by choosing $\Lambda = f_a, 4\pi f_a$. We noticed that the bounds on f_a overshoot the UV scale, if we take a similar approach to the KSVZ scenario. This completely invalidates the effective framework. As a result, all our bounds and projections for these two frameworks are given following the choice as mentioned before. We conclude from Figs. 17 and 18, that $f_a \sim 10^5$ GeV and 10^6 GeV can be ruled out using the present experimental data. For a Flaxion-like framework, the limits hardly change while changing the UV scale because the dominant contribution comes from the large tree-level Wilson coefficient, which are unchanged by $\mathcal{O}(\alpha_w)$ effects due to RGEs.

³In principle, axion flavor violating interactions with light quark fields might require further extension of the decay expressions presented in Appendix E. We don't consider such effects for the present analysis.

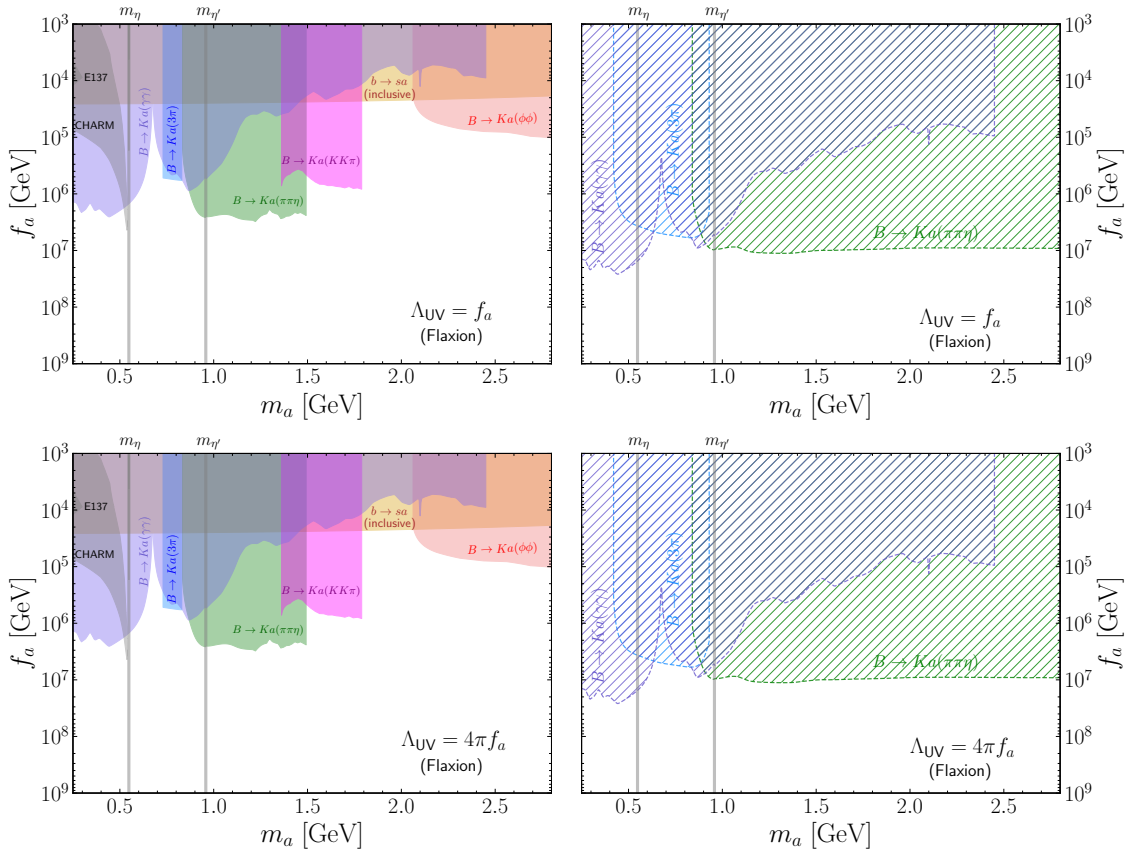


Figure 18. Limits on axion parameter space corresponding to the Flaxion model with the initial conditions of Eq. (8.10). As already discussed in the previous plots, the colors and the dashed curves represent the present and future projection bounds on the axion parameter space.

9 Conclusion

Heavy ALPs, with masses in the range of $\mathcal{O}(100) \text{ MeV} < m_a < \mathcal{O}(1) \text{ GeV}$, are well motivated because not only they can address the strong- CP problem but also ameliorate the axion quality problem. Such a region is also technically challenging, due to the difficulties in the rigorous perturbative computation of the $b \rightarrow s$ transition rate. Moreover, such an axion can also play an important role in explaining the matter-antimatter asymmetry of the universe. Searches for such an axion have gained much attention in the recent past, mostly from the perspective of novel signatures at intensity frontier experiments. In this work, we provide a comprehensive study of such an ALP and provide present bounds and future projections based on experiments such as Belle and BaBar, etc. Since we ignore any leptonic interactions of the axion, our focus mainly lies on hadronic production and decay modes of the axion along with the unavoidable $a \rightarrow \gamma\gamma$ channel.

We start with the KSVZ-like model where the axion only interacts with SM gluon fields, inducing flavor-changing neutral current processes at two-loop. Such diagrams usually have UV, UV-IR mix, and purely IR divergences. We show that appropriate counterterms,

viz. axion-quark diagonal and off-diagonal operators, eliminate both UV and UV-IR mix divergences. These counterterms are simply new operators at the UV, which renormalize the theory. Although all axion-quark off-diagonal operators are generated at the UV, our main focus is on operators that give rise to $b \rightarrow s$ transitions. We compute the anomalous dimension matrix at $\mathcal{O}(\alpha_s)$, $\mathcal{O}(\alpha_w)$, $\mathcal{O}(\alpha_t)$, and $\mathcal{O}(\alpha_s\alpha_w)$ (this two-loop contribution is dominant in heavy QCD axion scenarios). The $\mathcal{O}(\alpha_s^2)$ contributions, important for precision studies, only provide corrections to existing terms and do not generate any operators via operator mixing, so we ignore them. The Wilson coefficients are evolved from the UV scale to the electroweak scale M_W by the corresponding RGEs. Afterwards, we show that the pure IR divergences from two loops cancel upon matching with the effective theory below M_W . Throughout, we work in naive dimensional regularization with the $\overline{\text{MS}}$ scheme. Finally, we consider only prompt vertex searches of the ALP and provide bounds and future projections on the axion parameter space based on existing data and 3 ab^{-1} projected luminosity from Belle. We analyze different hadronic decay modes of the axion such as $a \rightarrow \pi\pi\eta$, $a \rightarrow KK\pi$ etc. For the KSVZ-like model and $\Lambda_{\text{UV}} = 1$ and 10 TeV , we observe that f_a values of 100 GeV and 1 TeV can be ruled out, respectively, using the present data set from the Belle and BaBar experiments. In addition, larger areas of the parameter space up to $f_a \sim 10 \text{ TeV}$ can also be probed with the projected luminosity of Belle II. Note that for all KSVZ bounds and projections, the axion only talks to SM gluon fields in the UV, and the initial values of all other Wilson coefficients are set to zero. We have checked that the limits are both quantitatively and qualitatively more or less robust if one introduces loop-induced values of the UV coefficients of other operators.

We show similar exclusions and projections for DFSZ and Flaxion frameworks as well. The UV values of the operators are motivated by [7, 73, 84]. Because of the presence of direct coupling between the axion and SM quark fields, one obtains stronger bounds for both these cases. It is important to note that the operator $b - s - a$ runs only at $\mathcal{O}(\alpha_w)$. Therefore, we notice negligible sensitivity to the UV scale in the Flaxion model. To conclude, for the DSFZ and Flaxion frameworks, the values of f_a that can be probed with the full luminosity of the Belle II data are 10^6 GeV and 10^7 GeV , respectively. In particular, for the DFSZ-like framework, certain islands have already been ruled out with $f_a \sim 1 \text{ TeV}$. This peculiar feature is an artifact of the variation of the Wilson coefficient \mathcal{C}'_{4L} as a function of f_a , as already discussed in the text.

Acknowledgments

We thank Joydeep Chakraborty, Manfred Kraus, Vazha Loladze, Takemichi Okui, Ennio Salvioni and Kohsaku Tobioka for discussions and valuable comments on the draft. SC thanks the Science and Engineering Research Board, Government of India (Grant No. SRG/2023/001162), and the IIT-Kanpur initiation grant (PHY/2022220) for financial support. SC also acknowledges the hospitality at ICTS, Bengaluru, during the ‘School for Advanced Topics in Particle Physics’ and TIFR, Mumbai, where part of the work was done.

A Interaction vertices

The following vertices arise from the terms $a - q_i - q_j$ and $a - G - \tilde{G}$ of the UV scale Lagrangian.

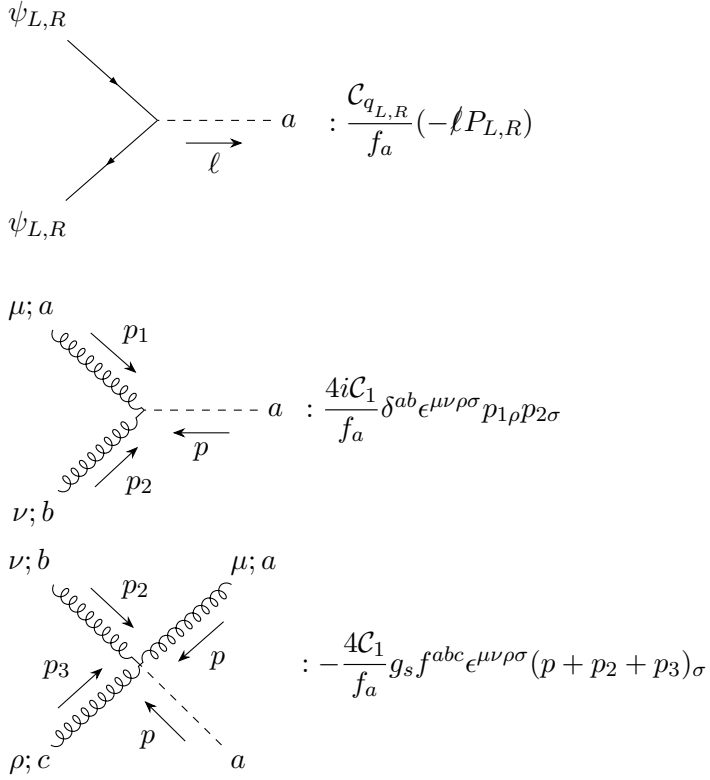


Figure 19. The vertex factors of relevant axion couplings with SM quarks and gluons.

B Example of a two-loop amplitude

In this appendix, we work out an explicit calculation illustrating the detailed steps we have employed to evaluate the two-loop 1PI diagrams in our analysis. We take the example of Fig. 20 as an illustration.

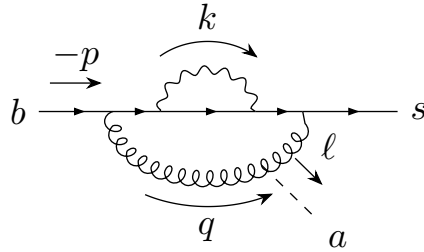


Figure 20. Illustrative example of a 1PI two-loop diagram contributing to $b \rightarrow sa$.

The amplitude for the $b \rightarrow sa$ process initiated by the $a - G - \tilde{G}$ coupling is written as

$$\begin{aligned}
i\Sigma_W^2 &= \left(\frac{ig}{\sqrt{2}}\right)^2 (ig_s)^2 \frac{4i\mathcal{C}_1}{f_a} C_F \delta_{ij} \sum_{q=u,c,t} V_{sq}^\dagger V_{qb} \int \frac{d^d k}{(2\pi)^d} \frac{d^d q}{(2\pi)^d} \gamma^\mu \frac{-ig_{\mu\mu'}}{(q-\ell)^2 - m_R^2} \\
&\times \epsilon^{\mu'\nu'\rho\sigma} (\ell - q)_\rho q_\sigma \frac{i(-\not{p} - \not{q})}{(p+q)^2 - m_R^2} \gamma^\alpha P_L \frac{i(-\not{p} - \not{k} - \not{q} + m_q)}{(p+k+q)^2 - m_q^2} \\
&\times \frac{-ig_{\nu\nu'} \gamma^{\nu'}}{q^2 - m_R^2} \frac{i(-\not{p} - \not{k} + m_q)}{(p+k)^2 - m_q^2} \gamma^\beta P_L \frac{-ig_{\alpha\beta}}{k^2 - M_W^2} . \tag{B.1}
\end{aligned}$$

We have taken the external light quark states, i.e., $m_s, m_b \rightarrow 0$, to be massless. This also induces an IR divergence. To properly obtain the UV poles, we have used a fictitious mass parameter m_R that acts as an IR regulator.

Feynman parameterization: The denominators are now clubbed via Feynman parameterization in the form

$$\frac{1}{[k'^2 - M^2(y)]^a} \frac{1}{[q'^2 - m_R^2]^b} \frac{1}{[(k'+q')^2 - m_q^2]^c} = \frac{1}{\mathcal{P}_1^a} \frac{1}{\mathcal{P}_2^b} \frac{1}{\mathcal{P}_3^c} = \mathcal{T}(a, b, c) . \tag{B.2}$$

Here y is the Feynman parameter and $M(y) = ym_q^2 + (1-y)M_W^2$ for the first three two-loop diagrams (Fig. 6) and $M(y) = M_W^2$ for the fourth diagram. To achieve this form (used for all two-loop integrals), we expand about the external momenta $p, \ell = 0$, where ℓ is the axion momentum. We only retain the leading-order term(s) that does not contain any powers of p and ℓ in the numerator (since we work in the approximation of vanishing external momenta). We have denoted the loop momenta by primes to convey that they may differ from the initial k, q momenta in the diagram after the Feynman parameterization. The corresponding substitution has to be made in the numerator $k \rightarrow k', q \rightarrow q'$. We now provide the details for the tensor reduction done after this substitution, denoting the new momenta as k, q .

Tensor reduction: Once the Dirac algebra of the numerator is done in d -dimensions, the tensorial quantities are reduced to scalar momenta dot products via the following expressions:

$$\begin{aligned}
T_{40}(q_\mu q_\nu q_\alpha q_\beta) &= \frac{(q \cdot q)^2}{d(d+2)} (\eta_{\mu\nu} \eta_{\alpha\beta} + \eta_{\mu\alpha} \eta_{\nu\beta} + \eta_{\mu\beta} \eta_{\nu\alpha}) , \\
T_{04}(k_\mu k_\nu k_\alpha k_\beta) &= \frac{(k \cdot k)^2}{d(d+2)} (\eta_{\mu\nu} \eta_{\alpha\beta} + \eta_{\mu\alpha} \eta_{\nu\beta} + \eta_{\mu\beta} \eta_{\nu\alpha}) , \\
T_{31}(q_\mu q_\nu q_\alpha k_\beta) &= \frac{(q \cdot q)(q \cdot k)}{d(d+2)} (\eta_{\mu\nu} \eta_{\alpha\beta} + \eta_{\mu\alpha} \eta_{\nu\beta} + \eta_{\mu\beta} \eta_{\nu\alpha}) , \\
T_{13}(k_\mu k_\nu k_\alpha q_\beta) &= \frac{(k \cdot k)(k \cdot q)}{d(d+2)} (\eta_{\mu\nu} \eta_{\alpha\beta} + \eta_{\mu\alpha} \eta_{\nu\beta} + \eta_{\mu\beta} \eta_{\nu\alpha}) , \\
T_{22}(q_\mu q_\nu k_\alpha k_\beta) &= A \eta_{\mu\nu} \eta_{\alpha\beta} + B \eta_{\mu\alpha} \eta_{\nu\beta} + C \eta_{\mu\beta} \eta_{\nu\alpha} , \\
T_{30}(q_\mu q_\nu q_\alpha) &= 0 , \quad T_{03}(k_\mu k_\nu k_\alpha) = 0 , \\
T_{02}(k_\alpha k_\beta) &= \frac{k \cdot k}{d} \eta_{\alpha\beta} , \quad T_{20}(q_\mu q_\nu) = \frac{q \cdot q}{d} \eta_{\mu\nu} , \quad T_{11}(q_\mu k_\alpha) = \frac{q \cdot k}{d} \eta_{\mu\alpha} ,
\end{aligned} \tag{B.3}$$

where the coefficients A, B and C can be obtained in a straightforward way by taking appropriate dot products with $\eta_{\star\star}$, where the \star 's denote appropriate Lorentz indices.

$$A = \frac{(1+d)k^2q^2 - 2(q.k)^2}{d(d-1)(d+2)}, \quad B = C = \frac{d(q.k)^2 - q^2k^2}{d(d-1)(d+2)}. \quad (\text{B.4})$$

Then, using (B.2), the following substitutions are made in the numerator

$$k.k = \mathcal{P}_1 + M^2, \quad q.q = \mathcal{P}_2 + m_R^2, \quad k.q = \frac{1}{2}(\mathcal{P}_3 - \mathcal{P}_2 - \mathcal{P}_1 + m_q^2 - M^2 - m_R^2). \quad (\text{B.5})$$

This converts every term in the two-loop integral to the form $\mathcal{T}(a, b, c)$ (multiplied by mass scales and numerical factors). Next, we use KIRA [100] for expressing these integrals on the basis of the four master integrals $\mathcal{T}(1, 1, 1)$, $\mathcal{T}(1, 0, 1)$, $\mathcal{T}(1, 1, 0)$, $\mathcal{T}(0, 1, 1)$.

Final evaluation: We now substitute the explicit expressions of these four master integrals. The result is expanded about $m_R = 0$. The leading order term in the series contains a logarithm of m_R and all higher order terms drop out in the limit $m_R \rightarrow 0$.

Thereby, we obtain the result for Fig. 20 as:

$$i\Sigma_W^2 = \kappa \left[\frac{1}{\epsilon^2} + \frac{1}{\epsilon} \left(2 \log \left(\frac{m_R^2}{M_W^2} \right) - \frac{5}{2} \right) \right] (-\not{P}_L). \quad (\text{B.6})$$

The result of the corresponding Goldstone diagram has to be added for the complete evaluation of the diagram. As mentioned in the text, the UV and UV-IR divergences go away due to the insertions of appropriate counterterms. However, we still have pure IR divergences, which we have shown explicitly cancel out as a result of matching with the EFT amplitude.

C Bounds for KSVZ-Like scenario ($\Lambda = 4\pi f_a$)

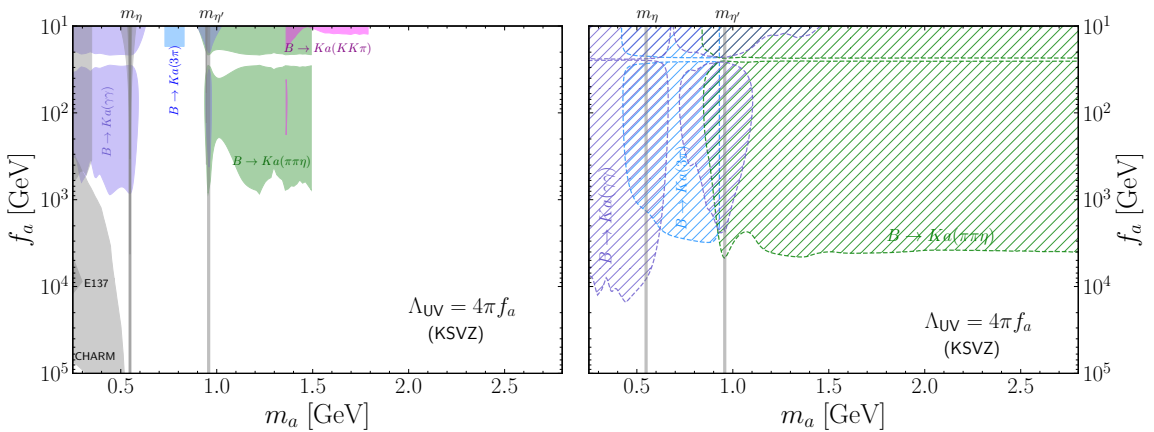


Figure 21. Bounds and projections for the KSVZ-like framework with the choice $\Lambda = 4\pi f_a$. The reasons for the island like features have already been discussed in the text, see Sec. 8.2.

D Input Parameters

In table 3, we collect the experimental values of the important parameters for numerical estimation from PDG-2024 [110].

Parameters	Values	Parameters	Values	Parameters	Values
G_F	$1.1664 \times 10^{-5} \text{ GeV}^{-2}$	M_W	80.369 GeV	M_Z	91.188 GeV
$\alpha_s(M_Z)$	0.118	$\alpha_w(M_W)$	0.339	$\alpha_e(M_Z)$	1/127.9
$\sin^2(\theta_W)$	0.231	m_B	5.28 GeV	m_K	0.498 GeV
m_d (2 GeV)	0.007 GeV	m_s (2 GeV)	0.12 GeV	m_b (m_b)	4.3 GeV
m_u (2 GeV)	0.003 GeV	m_c (m_c)	1.2 GeV	m_t (m_t)	162.69 GeV
m_t^{pole}	172.5 GeV	y_t (m_t^{pole})	1.150	v	246 GeV
V_{ud}	0.974	V_{us}	0.224	V_{ub}	0.004
V_{cd}	-0.221	V_{cs}	0.975	V_{cb}	0.0411
V_{td}	0.009	V_{ts}	-0.042	V_{tb}	1.010

Table 3. We present the values of the parameters used in our work.

E Axion decay width

The ALP Lagrangian, described in Eq. (5.1) can be further evolved down to $\mu_\chi = 1-2 \text{ GeV}$, where the only relevant degrees of freedom are the three light quarks, i.e. $q \equiv u, d, s$.

$$\begin{aligned} \mathcal{L}_{\text{eff}}(\mu_\chi) = & \frac{1}{2}(\partial_\mu a)^2 - \frac{m_a^2}{2} a^2 + \mathcal{C}_{gg} \frac{\alpha_s}{4\pi} \frac{a}{f_a} G_{\mu\nu}^b \tilde{G}^{\mu\nu,b} + \mathcal{C}_{\gamma\gamma} \frac{\alpha}{4\pi} \frac{a}{f_a} F_{\mu\nu} \tilde{F}^{\mu\nu} \\ & + \bar{q}(i\not{D} - \mathbf{m}_q)q + \frac{\partial_\mu a}{f_a} \bar{q} \mathcal{C}_{qq} \gamma^\mu \gamma_5 q, \end{aligned} \quad (\text{E.1})$$

where $\mathbf{m}_q = \text{diag}(m_u, m_d, m_s)$. For generality, we keep the term of the axion-photon interaction, but consider $\mathcal{C}_{\gamma\gamma} = 0$ for our analysis. Comparing with Eq. (2.1), $\mathcal{C}_1 = C_{gg} (\alpha_s/4\pi)$, with $C_{gg} = 1/2$. Furthermore, to facilitate matching with the Chiral Lagrangian, in this section, we neglect the $\mathcal{O}(\alpha_w)$ differences due to running in the left- and right-handed axion-quark Wilson coefficients at μ_χ . Hence, the γ_5 structure of these operators is used, without decomposing into P_L and P_R .

It is customary and convenient to rotate away the axion-gluon interaction by performing a chiral rotation on the quark fields given by

$$q \rightarrow \exp\left(-i\boldsymbol{\kappa}_q \mathcal{C}_{gg} \frac{a}{f_a} \gamma_5\right) q. \quad (\text{E.2})$$

Imposing the condition $\text{tr}(\boldsymbol{\kappa}_q) = 1$, where $\boldsymbol{\kappa}_q$ is a real 3×3 matrix, leads to the effective Lagrangian

$$\mathcal{L}_{\text{eff}}(\mu_\chi) = \frac{1}{2}(\partial_\mu a)^2 - \frac{m_a^2}{2} a^2 + \hat{\mathcal{C}}_{\gamma\gamma} \frac{\alpha}{4\pi} \frac{a}{f_a} F_{\mu\nu} \tilde{F}^{\mu\nu} + \bar{q}(i\not{D} - \hat{\mathbf{m}}_q)q + \frac{\partial_\mu a}{f_a} \bar{q} \hat{\mathcal{C}}_{qq} \gamma^\mu \gamma_5 q, \quad (\text{E.3})$$

where,

$$\begin{aligned}
\hat{\mathbf{m}}_q &= e^{-i\boldsymbol{\kappa}_q \mathcal{C}_{gg} a \gamma_5 / f_a} \mathbf{m}_q e^{-i\boldsymbol{\kappa}_q \mathcal{C}_{gg} a \gamma_5 / f_a}, \\
\hat{\mathcal{C}}_{qq} &= \mathcal{C}_{qq} + \mathcal{C}_{gg} \boldsymbol{\kappa}_q, \\
\hat{\mathcal{C}}_{\gamma\gamma} &= \mathcal{C}_{\gamma\gamma} - 2N_c \mathcal{C}_{gg} \sum_q Q_q^2 \boldsymbol{\kappa}_q.
\end{aligned} \tag{E.4}$$

The major advantage for such a chiral rotation is that the theory is now completely written in terms of the quark fields. As a result, it can be matched with an effective theory of mesons and baryons, such as the chiral Lagrangian. However, the interaction between the axion and vector mesons can be included in a phenomenological way through the vector meson dominance interactions. So, the Lagrangian is given by [52]

$$\begin{aligned}
\mathcal{L}_{\text{ChPT}} &= \frac{1}{2} \partial^\mu a \partial_\mu a - \frac{m_a^2}{2} a^2 + \frac{f_\pi^2}{8} \text{tr} [D^\mu \boldsymbol{\Sigma} D_\mu \boldsymbol{\Sigma}^\dagger] + \frac{f_\pi^2}{4} B_0 \text{tr} [\boldsymbol{\Sigma} \hat{\mathbf{m}}_q^\dagger + \hat{\mathbf{m}}_q \boldsymbol{\Sigma}^\dagger] \\
&+ \frac{i f_\pi^2}{4} \frac{\partial^\mu a}{f_a} \text{tr} [\hat{\mathcal{C}}_{qq} (\boldsymbol{\Sigma} D_\mu \boldsymbol{\Sigma}^\dagger - \boldsymbol{\Sigma}^\dagger D_\mu \boldsymbol{\Sigma})] + \hat{\mathcal{C}}_{\gamma\gamma} \frac{\alpha}{4\pi} \frac{a}{f_a} F_{\mu\nu} \tilde{F}^{\mu\nu} + \mathcal{L}_{\text{VMD}},
\end{aligned} \tag{E.5}$$

with,

$$\boldsymbol{\Sigma} = \exp(2i\mathbf{P}/f_\pi), \quad \mathbf{P} = \begin{pmatrix} \frac{\pi^0}{\sqrt{2}} + \frac{\eta}{\sqrt{3}} + \frac{\eta'}{\sqrt{6}} & \pi^+ & K^+ \\ \pi^- & -\frac{\pi^0}{\sqrt{2}} + \frac{\eta}{\sqrt{3}} + \frac{\eta'}{\sqrt{6}} & K^0 \\ K^- & \bar{K}^0 & -\frac{\eta}{\sqrt{3}} + \frac{2\eta'}{\sqrt{6}} \end{pmatrix}. \tag{E.6}$$

We consider f_π or the pion decay constant to be ~ 130 MeV. The chiral condensate parameter that captures the isospin-breaking effects is $B_0 \approx m_\pi^2 / (m_u + m_d)$, the covariant derivative also has the usual form $D_\mu \boldsymbol{\Sigma} = \partial_\mu \boldsymbol{\Sigma} - ie A_\mu [\mathbf{Q}, \boldsymbol{\Sigma}]$, where $\mathbf{Q} = \text{diag}(Q_u, Q_d, Q_s)$. The usual choice of $\boldsymbol{\kappa}_q = \mathbf{m}_q^{-1} / \text{tr}(\mathbf{m}_q^{-1})$ eliminates the mass mixing between axion and π^0, η_8 mesons. Furthermore, the physical η, η' are related to the octet and singlet fields by [110]

$$\begin{pmatrix} \eta \\ \eta' \end{pmatrix} = \begin{pmatrix} \cos \theta & -\sin \theta \\ \sin \theta & \cos \theta \end{pmatrix} \begin{pmatrix} \eta_8 \\ \eta_0 \end{pmatrix}, \quad \sin \theta \approx -\frac{1}{3}, \quad \cos \theta \approx \frac{2\sqrt{2}}{3}. \tag{E.7}$$

Finally, the vector meson dominance Lagrangian [111] is given by

$$\begin{aligned}
\mathcal{L}_{\text{VMD}} &= \frac{g_{VVP}}{2} \text{tr} (\mathbf{P} \mathbf{V}_{\mu\nu} \tilde{\mathbf{V}}^{\mu\nu}) + \frac{i N_c e}{6\pi^2 f_\pi^3} \epsilon^{\mu\nu\rho\sigma} A_\mu \text{tr} (\mathbf{Q} \partial_\nu \mathbf{P} \partial_\rho \mathbf{P} \partial_\sigma \mathbf{P}) \\
&+ f_\pi^2 \left[\text{tr} \left(\frac{g}{\sqrt{2}} \mathbf{V}_\mu - e A_\mu \mathbf{Q} - \frac{i}{2f_\pi^2} [\mathbf{P}, \partial_\mu \mathbf{P}] \right) \right]^2,
\end{aligned} \tag{E.8}$$

where the vector meson matrix is

$$\mathbf{V} = \begin{pmatrix} \frac{\rho_0 + \omega}{\sqrt{2}} & \rho^+ & K^{*+} \\ \rho^- & \frac{-\rho_0 + \omega}{\sqrt{2}} & K^{*0} \\ K^{*-} & \bar{K}^{*0} & \phi \end{pmatrix}, \quad \text{with } g_{VVP} = -\frac{N_c g^2}{8\pi^2 f_\pi}, \quad g = \frac{m_\rho}{f_\pi} \approx 6.0. \tag{E.9}$$

Diagonalization of the kinetic and mass term at the $\mathcal{O}(f_\pi/f_a)$ in the ChPT Lagrangian leads to a shift in the axion and meson fields by [45, 101, 112]

$$a \rightarrow a - \frac{f_\pi}{\sqrt{2}f_a} \sum_P \frac{m_P^2}{m_a^2} \text{tr}(\mathbf{aP})P, \quad P \rightarrow P + \frac{f_\pi}{\sqrt{2}f_a} \text{tr}(\mathbf{aP})a, \quad \text{tr}(\mathbf{aP}) = \frac{m_a^2 K_{aP}}{m_a^2 - m_P^2}, \quad (\text{E.10})$$

where $P = \pi^0, \eta, \eta'$, and K_{aP} is defined as

$$K_{a\pi^0} = \hat{C}_u - \hat{C}_d, \quad K_{a\eta} = \sqrt{\frac{2}{3}}(\hat{C}_u + \hat{C}_d - \hat{C}_s), \quad K_{a\eta'} = \frac{1}{\sqrt{3}}(\hat{C}_u + \hat{C}_d + 2\hat{C}_s). \quad (\text{E.11})$$

The effects of isospin breaking due to $m_u \neq m_d$ are neglected. Following the notation of [45], we assign the axion field in $U(3)$ representation as

$$\mathbf{a} = \sum_P \text{tr}(\mathbf{aP})P, \quad (\text{E.12})$$

where from (E.6), we see

$$\boldsymbol{\pi}^0 = \frac{1}{\sqrt{2}} \text{diag}(1, -1, 0), \quad \boldsymbol{\eta} = \frac{1}{\sqrt{3}} \text{diag}(1, 1, -1), \quad \boldsymbol{\eta}' = \frac{1}{\sqrt{6}} \text{diag}(1, 1, 2). \quad (\text{E.13})$$

We use the above definitions in the decay width expressions given by

$$\begin{aligned} \Gamma_{a \rightarrow \gamma\gamma} &= \frac{\alpha^2 m_a^3}{(4\pi)^3 f_a^2} \left| C_\gamma^{\text{rot}} + C_\gamma^{\text{VMD}} + C_\gamma^{\text{pQCD},uds} + C_\gamma^{\text{pQCD},cbt} \right|^2 \\ \Gamma_{a \rightarrow \phi\phi} &= \frac{N_c^2}{2048\pi^5} \frac{m_a^3}{f_a^2} |g^2 \text{tr}(\mathbf{a}\phi\phi)\mathcal{F}(m_a)|^2 \left(1 - \frac{4m_\phi^2}{m_a^2}\right)^{3/2}, \\ \Gamma_{a \rightarrow 3\text{-body}} &= \frac{1}{32(2\pi)^3 S m_a^3} \int dm_{12}^2 dm_{23}^2 |\overline{\mathcal{M}}_{a \rightarrow 3\text{-body}}|^2, \end{aligned} \quad (\text{E.14})$$

where S is the symmetry factor and $m_{ij}^2 = (p_i + p_j)^2$, with $p_{i,j}$ denoting the momenta of the final-state particles. The Chiral rotation contribution in $\hat{C}_{\gamma\gamma}$ gives

$$C_\gamma^{\text{rot}} = 2N_c \mathcal{C}_{gg} \sum_{q=u,d,s} Q_q^2 \kappa_q \Theta(m_{\eta'} - m_a), \quad (\text{E.15})$$

The expressions for other Wilson coefficients in $\Gamma_{a \rightarrow \gamma\gamma}$ and amplitude expressions \mathcal{M} for three body decay modes are explicitly given in Ref. [101]. The different inputs presented in [45, 101] can be used in the above expressions with the following replacements

$$f_\pi \rightarrow f_\pi/\sqrt{2}, \quad \langle \mathbf{aP} \rangle \rightarrow \text{tr}(\mathbf{aP}), \quad \langle \mathbf{aVV} \rangle \rightarrow \frac{1}{\sqrt{2}} \text{tr}(\mathbf{aVV}), \quad (\text{E.16})$$

which converts their definitions (LHS) to ours (RHS). Finally, the meson masses, decay widths, and relevant meson couplings are taken from [110, 113, 114].

References

- [1] S. Weinberg, *A New Light Boson?*, *Phys. Rev. Lett.* **40** (1978) 223.
- [2] F. Wilczek, *Problem of Strong P and T Invariance in the Presence of Instantons*, *Phys. Rev. Lett.* **40** (1978) 279.
- [3] R.D. Peccei and H.R. Quinn, *CP Conservation in the Presence of Instantons*, *Phys. Rev. Lett.* **38** (1977) 1440.
- [4] R.D. Peccei and H.R. Quinn, *Constraints Imposed by CP Conservation in the Presence of Instantons*, *Phys. Rev. D* **16** (1977) 1791.
- [5] G. 't Hooft, *Symmetry Breaking Through Bell-Jackiw Anomalies*, *Phys. Rev. Lett.* **37** (1976) 8.
- [6] J. Preskill, M.B. Wise and F. Wilczek, *Cosmology of the Invisible Axion*, *Phys. Lett. B* **120** (1983) 127.
- [7] M. Dine and W. Fischler, *The Not So Harmless Axion*, *Phys. Lett. B* **120** (1983) 137.
- [8] L.F. Abbott and P. Sikivie, *A Cosmological Bound on the Invisible Axion*, *Phys. Lett. B* **120** (1983) 133.
- [9] R.T. Co and K. Harigaya, *Axiogenesis*, *Phys. Rev. Lett.* **124** (2020) 111602 [[1910.02080](#)].
- [10] S. Chakraborty, T.H. Jung and T. Okui, *Composite neutrinos and the QCD axion: Baryogenesis, dark matter, small Dirac neutrino masses, and vanishing neutron electric dipole moment*, *Phys. Rev. D* **105** (2022) 015024 [[2108.04293](#)].
- [11] P.W. Graham, D.E. Kaplan and S. Rajendran, *Cosmological Relaxation of the Electroweak Scale*, *Phys. Rev. Lett.* **115** (2015) 221801 [[1504.07551](#)].
- [12] A. Hook and G. Marques-Tavares, *Relaxation from particle production*, *JHEP* **12** (2016) 101 [[1607.01786](#)].
- [13] S. Trifinopoulos and M. Vanvlasselaer, *Attracting the electroweak scale to a tachyonic trap*, *Phys. Rev. D* **107** (2023) L071701 [[2210.13484](#)].
- [14] A. Hook, S. Kumar, Z. Liu and R. Sundrum, *High Quality QCD Axion and the LHC*, *Phys. Rev. Lett.* **124** (2020) 221801 [[1911.12364](#)].
- [15] CAST collaboration, *New CAST Limit on the Axion-Photon Interaction*, *Nature Phys.* **13** (2017) 584 [[1705.02290](#)].
- [16] G.G. Raffelt, *Astrophysical axion bounds*, *Lect. Notes Phys.* **741** (2008) 51 [[hep-ph/0611350](#)].
- [17] A. Friedland, M. Giannotti and M. Wise, *Constraining the Axion-Photon Coupling with Massive Stars*, *Phys. Rev. Lett.* **110** (2013) 061101 [[1210.1271](#)].
- [18] A. Caputo and G. Raffelt, *Astrophysical Axion Bounds: The 2024 Edition*, *PoS COSMICWISPers* (2024) 041 [[2401.13728](#)].
- [19] CHARM collaboration, *Search for Axion Like Particle Production in 400-GeV Proton - Copper Interactions*, *Phys. Lett. B* **157** (1985) 458.
- [20] J.D. Bjorken, S. Ecklund, W.R. Nelson, A. Abashian, C. Church, B. Lu et al., *Search for Neutral Metastable Penetrating Particles Produced in the SLAC Beam Dump*, *Phys. Rev. D* **38** (1988) 3375.

- [21] J. Blumlein et al., *Limits on neutral light scalar and pseudoscalar particles in a proton beam dump experiment*, *Z. Phys. C* **51** (1991) 341.
- [22] B. Döbrich, J. Jaeckel, F. Kahlhoefer, A. Ringwald and K. Schmidt-Hoberg, *ALPtraum: ALP production in proton beam dump experiments*, *JHEP* **02** (2016) 018 [[1512.03069](#)].
- [23] M. Kamionkowski and J. March-Russell, *Planck scale physics and the Peccei-Quinn mechanism*, *Phys. Lett. B* **282** (1992) 137 [[hep-th/9202003](#)].
- [24] R. Holman, S.D.H. Hsu, T.W. Kephart, E.W. Kolb, R. Watkins and L.M. Widrow, *Solutions to the strong CP problem in a world with gravity*, *Phys. Lett. B* **282** (1992) 132 [[hep-ph/9203206](#)].
- [25] S.M. Barr and D. Seckel, *Planck scale corrections to axion models*, *Phys. Rev. D* **46** (1992) 539.
- [26] S. Ghigna, M. Lusignoli and M. Roncadelli, *Instability of the invisible axion*, *Phys. Lett. B* **283** (1992) 278.
- [27] S. Dimopoulos, *A Solution of the Strong CP Problem in Models With Scalars*, *Phys. Lett. B* **84** (1979) 435.
- [28] B. Holdom and M.E. Peskin, *Raising the Axion Mass*, *Nucl. Phys. B* **208** (1982) 397.
- [29] M. Dine and N. Seiberg, *String Theory and the Strong CP Problem*, *Nucl. Phys. B* **273** (1986) 109.
- [30] J.M. Flynn and L. Randall, *A Computation of the Small Instanton Contribution to the Axion Potential*, *Nucl. Phys. B* **293** (1987) 731.
- [31] K. Choi, C.W. Kim and W.K. Sze, *Mass Renormalization by Instantons and the Strong CP Problem*, *Phys. Rev. Lett.* **61** (1988) 794.
- [32] V.A. Rubakov, *Grand unification and heavy axion*, *JETP Lett.* **65** (1997) 621 [[hep-ph/9703409](#)].
- [33] K. Choi and H.D. Kim, *Small instanton contribution to the axion potential in supersymmetric models*, *Phys. Rev. D* **59** (1999) 072001 [[hep-ph/9809286](#)].
- [34] Z. Berezhiani, L. Gianfagna and M. Giannotti, *Strong CP problem and mirror world: The Weinberg-Wilczek axion revisited*, *Phys. Lett. B* **500** (2001) 286 [[hep-ph/0009290](#)].
- [35] K.-w. Choi, *A QCD axion from higher dimensional gauge field*, *Phys. Rev. Lett.* **92** (2004) 101602 [[hep-ph/0308024](#)].
- [36] A. Hook, *Anomalous solutions to the strong CP problem*, *Phys. Rev. Lett.* **114** (2015) 141801 [[1411.3325](#)].
- [37] H. Fukuda, K. Harigaya, M. Ibe and T.T. Yanagida, *Model of visible QCD axion*, *Phys. Rev. D* **92** (2015) 015021 [[1504.06084](#)].
- [38] S. Dimopoulos, A. Hook, J. Huang and G. Marques-Tavares, *A collider observable QCD axion*, *JHEP* **11** (2016) 052 [[1606.03097](#)].
- [39] P. Agrawal and K. Howe, *Factoring the Strong CP Problem*, *JHEP* **12** (2018) 029 [[1710.04213](#)].
- [40] P. Agrawal, G. Marques-Tavares and W. Xue, *Opening up the QCD axion window*, *JHEP* **03** (2018) 049 [[1708.05008](#)].

- [41] M.K. Gaillard, M.B. Gavela, R. Houtz, P. Quilez and R. Del Rey, *Color unified dynamical axion*, *Eur. Phys. J. C* **78** (2018) 972 [[1805.06465](#)].
- [42] T. Gherghetta, V.V. Khoze, A. Pomarol and Y. Shirman, *The Axion Mass from 5D Small Instantons*, *JHEP* **03** (2020) 063 [[2001.05610](#)].
- [43] R.S. Gupta, V.V. Khoze and M. Spannowsky, *Small instantons and the strong CP problem in composite Higgs models*, *Phys. Rev. D* **104** (2021) 075011 [[2012.00017](#)].
- [44] A. Delgado and S. Koren, *Non-Invertible Peccei-Quinn Symmetry, Natural 2HDM Alignment, and the Visible Axion*, [2412.05362](#).
- [45] D. Aloni, Y. Soreq and M. Williams, *Coupling QCD-Scale Axionlike Particles to Gluons*, *Phys. Rev. Lett.* **123** (2019) 031803 [[1811.03474](#)].
- [46] G. Grilli di Cortona, E. Hardy, J. Pardo Vega and G. Villadoro, *The QCD axion, precisely*, *JHEP* **01** (2016) 034 [[1511.02867](#)].
- [47] M. Bauer, M. Neubert, S. Renner, M. Schnubel and A. Thamm, *Consistent Treatment of Axions in the Weak Chiral Lagrangian*, *Phys. Rev. Lett.* **127** (2021) 081803 [[2102.13112](#)].
- [48] T. Bandyopadhyay, S. Ghosh and T.S. Roy, *ALP-Pions generalized*, *Phys. Rev. D* **105** (2022) 115039 [[2112.13147](#)].
- [49] PIENU collaboration, *Search for heavy neutrinos in $\pi \rightarrow \mu\nu$ decay*, *Phys. Lett. B* **798** (2019) 134980 [[1904.03269](#)].
- [50] D. Pocanic et al., *Precise measurement of the $\pi^+ \rightarrow \pi^0 e^+ \nu$ branching ratio*, *Phys. Rev. Lett.* **93** (2004) 181803 [[hep-ex/0312030](#)].
- [51] W. Altmannshofer, S. Gori and D.J. Robinson, *Constraining axionlike particles from rare pion decays*, *Phys. Rev. D* **101** (2020) 075002 [[1909.00005](#)].
- [52] H. Georgi, D.B. Kaplan and L. Randall, *Manifesting the Invisible Axion at Low-energies*, *Phys. Lett. B* **169** (1986) 73.
- [53] W.A. Bardeen, R.D. Peccei and T. Yanagida, *CONSTRAINTS ON VARIANT AXION MODELS*, *Nucl. Phys. B* **279** (1987) 401.
- [54] D.S.M. Alves and N. Weiner, *A viable QCD axion in the MeV mass range*, *JHEP* **07** (2018) 092 [[1710.03764](#)].
- [55] S. Gori, G. Perez and K. Tobioka, *KOTO vs. NA62 Dark Scalar Searches*, *JHEP* **08** (2020) 110 [[2005.05170](#)].
- [56] E949 collaboration, *Search for the decay K^+ to π^+ gamma gamma in the π^+ momentum region $P > 213$ MeV/c*, *Phys. Lett. B* **623** (2005) 192 [[hep-ex/0505069](#)].
- [57] NA62 collaboration, *Study of the $K^\pm \rightarrow \pi^\pm \gamma\gamma$ decay by the NA62 experiment*, *Phys. Lett. B* **732** (2014) 65 [[1402.4334](#)].
- [58] KTeV collaboration, *Final Results from the KTeV Experiment on the Decay $K_L \rightarrow \pi^0 \gamma\gamma$* , *Phys. Rev. D* **77** (2008) 112004 [[0805.0031](#)].
- [59] KOTO collaboration, *Search for the $K_L \rightarrow \pi^0 \nu\bar{\nu}$ and $K_L \rightarrow \pi^0 X^0$ decays at the J-PARC KOTO experiment*, *Phys. Rev. Lett.* **122** (2019) 021802 [[1810.09655](#)].
- [60] GLUEX collaboration, *Measurement of the beam asymmetry Σ for π^0 and η photoproduction on the proton at $E_\gamma = 9$ GeV*, *Phys. Rev. C* **95** (2017) 042201 [[1701.08123](#)].

- [61] D. Aloni, C. Fanelli, Y. Soreq and M. Williams, *Photoproduction of Axionlike Particles*, *Phys. Rev. Lett.* **123** (2019) 071801 [[1903.03586](#)].
- [62] OPAL collaboration, *Multiphoton production in e^+e^- collisions at $s^{*(1/2)} = 181\text{-GeV}$ to 209-GeV* , *Eur. Phys. J. C* **26** (2003) 331 [[hep-ex/0210016](#)].
- [63] S. Knapen, T. Lin, H.K. Lou and T. Melia, *Searching for Axionlike Particles with Ultraperipheral Heavy-Ion Collisions*, *Phys. Rev. Lett.* **118** (2017) 171801 [[1607.06083](#)].
- [64] M. Bauer, M. Neubert and A. Thamm, *Collider Probes of Axion-Like Particles*, *JHEP* **12** (2017) 044 [[1708.00443](#)].
- [65] CMS collaboration, *Search for low mass vector resonances decaying into quark-antiquark pairs in proton-proton collisions at $\sqrt{s} = 13\text{ TeV}$* , *JHEP* **01** (2018) 097 [[1710.00159](#)].
- [66] A. Mariotti, D. Redigolo, F. Sala and K. Tobioka, *New LHC bound on low-mass diphoton resonances*, *Phys. Lett. B* **783** (2018) 13 [[1710.01743](#)].
- [67] T. Biswas, *Probing the interactions of axion-like particles with electroweak bosons and the Higgs boson in the high energy regime at LHC*, *JHEP* **05** (2024) 081 [[2312.05992](#)].
- [68] S.-s. Bao, W. Gao, H. Zhang and J. Zhou, *Constraining Axion-Gluon Coupling in Mono-hadron Processes*, [2405.18215](#).
- [69] M. Bauer, M. Neubert, S. Renner, M. Schnubel and A. Thamm, *The Low-Energy Effective Theory of Axions and ALPs*, *JHEP* **04** (2021) 063 [[2012.12272](#)].
- [70] M. Bauer, M. Neubert, S. Renner, M. Schnubel and A. Thamm, *Flavor probes of axion-like particles*, *JHEP* **09** (2022) 056 [[2110.10698](#)].
- [71] S. Chakraborty, M. Kraus, V. Loladze, T. Okui and K. Tobioka, *Heavy QCD axion in $b \rightarrow s$ transition: Enhanced limits and projections*, *Phys. Rev. D* **104** (2021) 055036 [[2102.04474](#)].
- [72] E. Bertholet, S. Chakraborty, V. Loladze, T. Okui, A. Soffer and K. Tobioka, *Heavy QCD axion at Belle II: Displaced and prompt signals*, *Phys. Rev. D* **105** (2022) L071701 [[2108.10331](#)].
- [73] Y. Ema, K. Hamaguchi, T. Moroi and K. Nakayama, *Flaxion: a minimal extension to solve puzzles in the standard model*, *JHEP* **01** (2017) 096 [[1612.05492](#)].
- [74] PLANCK collaboration, *Planck 2015 results. XIII. Cosmological parameters*, *Astron. Astrophys.* **594** (2016) A13 [[1502.01589](#)].
- [75] J. Martin Camalich, M. Pospelov, P.N.H. Vuong, R. Ziegler and J. Zupan, *Quark Flavor Phenomenology of the QCD Axion*, *Phys. Rev. D* **102** (2020) 015023 [[2002.04623](#)].
- [76] T. Li, Z. Qian, M.A. Schmidt and M. Yuan, *The quark flavor-violating ALPs in light of B mesons and hadron colliders*, *JHEP* **05** (2024) 232 [[2402.14232](#)].
- [77] A. Greljo, A. Smolkovič and A. Valenti, *Froggatt-Nielsen ALP*, [2407.02998](#).
- [78] C.D. Froggatt and H.B. Nielsen, *Hierarchy of Quark Masses, Cabibbo Angles and CP Violation*, *Nucl. Phys. B* **147** (1979) 277.
- [79] A. Carmona, C. Scherb and P. Schwaller, *Charming ALPs*, *JHEP* **08** (2021) 121 [[2101.07803](#)].
- [80] E. Izaguirre, T. Lin and B. Shuve, *Searching for Axionlike Particles in Flavor-Changing Neutral Current Processes*, *Phys. Rev. Lett.* **118** (2017) 111802 [[1611.09355](#)].

- [81] M.B. Gavela, R. Houtz, P. Quilez, R. Del Rey and O. Sumensari, *Flavor constraints on electroweak ALP couplings*, *Eur. Phys. J. C* **79** (2019) 369 [[1901.02031](#)].
- [82] J.E. Kim, *Weak Interaction Singlet and Strong CP Invariance*, *Phys. Rev. Lett.* **43** (1979) 103.
- [83] M.A. Shifman, A.I. Vainshtein and V.I. Zakharov, *Can Confinement Ensure Natural CP Invariance of Strong Interactions?*, *Nucl. Phys. B* **166** (1980) 493.
- [84] M. Dine, W. Fischler and M. Srednicki, *A Simple Solution to the Strong CP Problem with a Harmless Axion*, *Phys. Lett. B* **104** (1981) 199.
- [85] A.R. Zhitnitsky, *On Possible Suppression of the Axion Hadron Interactions. (In Russian)*, *Sov. J. Nucl. Phys.* **31** (1980) 260.
- [86] A. Lella, E. Ravensburg, P. Carenza and M.C.D. Marsh, *Supernova limits on 'QCD axion-like particles'*, [2405.00153](#).
- [87] S. Chakraborty, A. Gupta and M. Vanvlasselaer, *Photo-production of axions in Supernovae*, [2403.12169](#).
- [88] Y. Bai, T.-K. Chen, J. Liu and X. Ma, *Wess-Zumino-Witten Interactions of Axions*, [2406.11948](#).
- [89] J.A. Harvey, C.T. Hill and R.J. Hill, *Anomaly mediated neutrino-photon interactions at finite baryon density*, *Phys. Rev. Lett.* **99** (2007) 261601 [[0708.1281](#)].
- [90] J.A. Harvey, C.T. Hill and R.J. Hill, *Standard Model Gauging of the Wess-Zumino-Witten Term: Anomalies, Global Currents and pseudo-Chern-Simons Interactions*, *Phys. Rev. D* **77** (2008) 085017 [[0712.1230](#)].
- [91] S. Chakraborty, A. Gupta and M. Vanvlasselaer, *Anomaly induced cooling of neutron stars: a Standard Model contribution*, *JCAP* **10** (2023) 030 [[2306.15872](#)].
- [92] A.J. Buras, M. Jamin and M.E. Lautenbacher, *Two loop anomalous dimension matrix for Delta S = 1 weak nonleptonic decays. 2. O(alpha-alpha-s)*, *Nucl. Phys. B* **400** (1993) 75 [[hep-ph/9211321](#)].
- [93] A. Buras, *Gauge Theory of Weak Decays*, Cambridge University Press (6, 2020), [10.1017/9781139524100](#).
- [94] A. Pich, *Effective field theory: Course*, in *Les Houches Summer School in Theoretical Physics, Session 68: Probing the Standard Model of Particle Interactions*, pp. 949–1049, 6, 1998 [[hep-ph/9806303](#)].
- [95] A.J. Buras and P.H. Weisz, *QCD Nonleading Corrections to Weak Decays in Dimensional Regularization and 't Hooft-Veltman Schemes*, *Nucl. Phys. B* **333** (1990) 66.
- [96] G. 't Hooft and M.J.G. Veltman, *Regularization and Renormalization of Gauge Fields*, *Nucl. Phys. B* **44** (1972) 189.
- [97] S. Chakraborty, D. Bisht and A. Samanta, *In preparation*, .
- [98] J.C. Collins, *Renormalization*, vol. 26 of *Cambridge Monographs on Mathematical Physics*, Cambridge University Press, Cambridge (7, 2023), [10.1017/9781009401807](#).
- [99] B. Ruijl, T. Ueda and J. Vermaseren, *FORM version 4.2*, [1707.06453](#).
- [100] P. Maierhöfer, J. Usovitsch and P. Uwer, *Kira—A Feynman integral reduction program*, *Comput. Phys. Commun.* **230** (2018) 99 [[1705.05610](#)].

- [101] H.-C. Cheng, L. Li and E. Salvioni, *A theory of dark pions*, *JHEP* **01** (2022) 122 [[2110.10691](#)].
- [102] PARTICLE DATA GROUP collaboration, *Review of Particle Physics*, *PTEP* **2020** (2020) 083C01.
- [103] BABAR collaboration, *Search for an Axionlike Particle in B Meson Decays*, *Phys. Rev. Lett.* **128** (2022) 131802 [[2111.01800](#)].
- [104] BABAR collaboration, *Study of B Meson Decays with Excited eta and eta-prime Mesons*, *Phys. Rev. Lett.* **101** (2008) 091801 [[0804.0411](#)].
- [105] LHCb collaboration, *Study of B_c^+ decays to the $K^+K^-\pi^+$ final state and evidence for the decay $B_c^+ \rightarrow \chi_{c0}\pi^+$* , *Phys. Rev. D* **94** (2016) 091102 [[1607.06134](#)].
- [106] BABAR collaboration, *Measurements of branching fractions and CP asymmetries and studies of angular distributions for $B \rightarrow \phi \phi K$ decays*, *Phys. Rev. D* **84** (2011) 012001 [[1105.5159](#)].
- [107] BELLE collaboration, *Measurement of branching fractions and CP violation parameters in $B \rightarrow \omega K$ decays with first evidence of CP violation in $B^0 \rightarrow \omega K_S^0$* , *Phys. Rev. D* **90** (2014) 012002 [[1311.6666](#)].
- [108] BABAR collaboration, *Belle ii $m_{\gamma\gamma}$ plots*, .
- [109] BABAR collaboration, *Search for the Decay $D^{0-} \rightarrow \gamma\gamma$ and Measurement of the Branching Fraction for $D^{0-} \rightarrow \pi^0\pi^0$* , *Phys. Rev. D* **85** (2012) 091107 [[1110.6480](#)].
- [110] PARTICLE DATA GROUP collaboration, *Review of particle physics*, *Phys. Rev. D* **110** (2024) 030001.
- [111] T. Fujiwara, T. Kugo, H. Terao, S. Uehara and K. Yamawaki, *Nonabelian Anomaly and Vector Mesons as Dynamical Gauge Bosons of Hidden Local Symmetries*, *Prog. Theor. Phys.* **73** (1985) 926.
- [112] G. Dalla Valle Garcia, F. Kahlhoefer, M. Ovchinnikov and A. Zaporozhchenko, *Phenomenology of axionlike particles with universal fermion couplings revisited*, *Phys. Rev. D* **109** (2024) 055042 [[2310.03524](#)].
- [113] A.H. Fariborz and J. Schechter, *$\eta' \rightarrow \eta\pi\pi$ decay as a probe of a possible lowest lying scalar nonet*, *Phys. Rev. D* **60** (1999) 034002 [[hep-ph/9902238](#)].
- [114] BABAR collaboration, *Measurement of the $I=1/2$ $K\pi$ \mathcal{S} -wave amplitude from Dalitz plot analyses of $\eta_c \rightarrow K\bar{K}\pi$ in two-photon interactions*, *Phys. Rev. D* **93** (2016) 012005 [[1511.02310](#)].